electronics

MDPI

Article

A Dual-Frequency Switchable LCC-S-S and S-S-S Compensated Three-Coil Topology with CC/CV Outputs and ZVS Operation for WPT Applications

Yafei Chen [1], Cunxin Wang [1], Dadi Sun [2], Kuncheng Wang [2], Dong-Hee Kim [3] and Guangyao Li [2,*]

[1] College of Electrical and Information Engineering, Zhengzhou University of Light Industry, Zhengzhou 450002, China; 2020034@zzuli.edu.cn (Y.C.); 332401010017@zzuli.edu.cn (C.W.)
[2] Zhengzhou Advanced Research Institute of Harbin Institute of Technology, Zhengzhou 450000, China; 26b306022@stu.hit.edu.cn (D.S.); 2021110532@stu.hit.edu.cn (K.W.)
[3] Department of Electrical Engineering, Chonnam National University, Gwangju 61186, Republic of Korea; kimdonghee@jnu.ac.kr
* Correspondence: liguangyao@hitzri.cn; Tel.: +86-19862951008

Abstract

Compared with conventional two-coil wireless power transfer (WPT) systems, three-coil WPT systems with an intermediate relay coil offer superior performance in terms of transmission distance and tuning flexibility, making them suitable for a wider range of applications. To address the CC/CV hybrid charging challenge in practical three-coil wireless power transfer (WPT) systems, based on the dual-frequency compensation network (DFCN), this paper proposes a dual-frequency switchable LCC-S-S and S-S-S compensated three-coil topology along with a systematic parameter tuning methodology. Furthermore, the proposed system exhibits zero-phase angle (ZPA) input impedance characteristics at both resonant frequencies, and the ZPA condition remains invariant under coupling coefficient variations. Unlike conventional approaches requiring additional active components, such as relays or AC switches, the proposed compensation topology realizes simple and efficient CC/CV hybrid charging by only switching between two resonant frequencies. An experimental prototype rated at 400 W is constructed to assess the efficacy of the presented framework. The system has a simple structure, is easy to control, and has stable output. The peak DC-DC efficiency reaches 92.15% and 92.75% in both the CC and CV charging modes, respectively.

Keywords: wireless power transfer (WPT); LCC-S-S and S-S-S compensated three-coil topology; dual-frequency compensation network (DFCN); constant current/constant voltage (CC/CV); zero-phase angle (ZPA)

Check for updates

Academic Editor: Jiangtao Huangfu

Received: 25 August 2026
Revised: 14 September 2026
Accepted: 16 September 2026
Published: 19 September 2026

1. Introduction

Conventional wired charging methods suffer from certain limitations in terms of safety and space utilization. Fueled by recent breakthroughs in power electronics and automatic control technologies, wireless power transfer (WPT) technology has achieved significant advances in recent years. Compared with conventional wired charging methods, WPT technology has been widely recognized by both academia and industry attributable to its multifaceted advantages spanning secure operation, user convenience, environmental viability, and consistent reliability [1,2]. Based on different coupling mechanisms, WPT systems can be broadly divided into inductive power transfer (IPT) and capacitive power transfer (CPT) [3,4]. Owing to its high technological maturity and strong applicability, IPT has been widely adopted in various applications, such as electric vehicle charging [5], mobile electronic devices [6], implantable medical devices [7,8], unmanned aerial vehicles [9] and wearable portable devices [10].

The load of a WPT system is typically a lithium-ion battery, whose typical charging characteristics are illustrated in Figure 1. Constant current (CC) charging and constant voltage (CV) charging constitute the two fundamental phases of a standard battery charging protocol. During the CC charging stage, the battery is charged at a preset constant current, causing the battery voltage to increase rapidly. Once the battery voltage reaches the specified threshold, the charging process transitions to the CV charging stage, where the charging current gradually decreases. Once the current decreases below the preset cut-off limit, the charging operation ceases. Dynamically, the equivalent load resistance of the battery increases nonlinearly as charging proceeds. Consequently, realizing CC/CV hybrid charging in WPT systems under variable load conditions has become a critical practical issue for the further application of WPT technology.

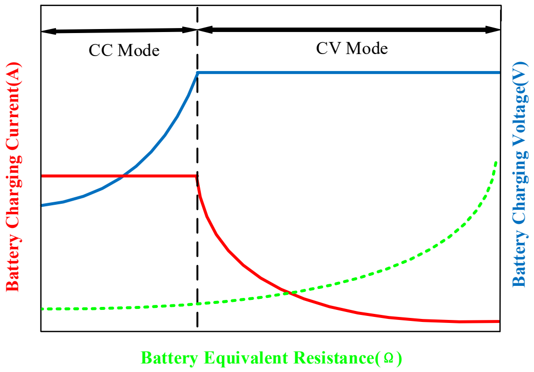

Figure 1. Typical CC/CV charging characteristics of a lithium-ion battery.

In WPT systems, the resonant compensation topology plays a crucial role, as its structure and parameters directly determine system performance in terms of output characteristics, transmission efficiency, power transfer capability, and other related aspects. The resonant compensation topology should exhibit zero-phase angle (ZPA) characteristics under resonant conditions to reduce reactive power losses and improve the power transfer capability of the system. Furthermore, the output characteristics of the resonant compensation topology should exhibit load-independent CC or CV characteristics to meet the requirements of battery charging applications. Currently, the series–series (S-S), series–parallel (S-P), parallel–series (P-S), and parallel–parallel (P-P) compensation topologies are widely adopted as fundamental resonant compensation structures in WPT systems [11]. Although these topologies offer advantages of simple structures and ease of design, their output characteristics are highly sensitive to the coupling conditions and resonant compensation parameters, leading to limited degrees of freedom for parameter tuning. To overcome these limitations, researchers have proposed various high-order compensation topologies, including S-SP [12], LCC-P [13], LCC-S [14], and dual-sided LCC (LCC-LCC) [15]. These topologies significantly enhance the performance and application potential of WPT systems. Conventional resonant compensation topologies can generally achieve only a single CC or CV output characteristic under resonant conditions, which limits their ability to meet the requirements of CC/CV hybrid charging in WPT systems.

Currently, there are mainly three approaches to achieving CC/CV hybrid output and ZPA operation in WPT systems:

(1) Additional DC/DC converters: In [16,17], an additional DC/DC converter is introduced at the output stage to regulate the output voltage/current. Although this

approach enables both CC/CV charging and ZPA operation, the multi-stage power conversion structure significantly increases the conduction losses and hardware complexity of WPT systems.

(2) Phase-shift modulation (PSM) and frequency conversion control (FCC): In [18–20], a hybrid PSM-FCC strategy is proposed to achieve CC/CV output and zero voltage switching (ZVS) operation by jointly regulating the inverter phase-shift angle and switching frequency. However, the coupling between the two control variables increases the complexity of the control algorithm and deteriorates the dynamic response. Furthermore, the frequency modulation process may drive the system away from the ZPA operating point, resulting in additional reactive power losses.

(3) Compensation topology reconstruction: In [21,22], conventional compensation topologies are dynamically reconfigured by incorporating AC switches (ACSs) and passive resonant compensation components to achieve CC/CV output and ZPA operation in WPT systems. Nevertheless, the multiple ACSs are typically distributed on both the transmitter and receiver sides, requiring strict timing synchronization during switching operations. This considerably complicates the control strategy and increases the overall system complexity. In addition, the introduced ACSs cause additional switching and conduction losses, which degrade the system efficiency.

The aforementioned approaches for realizing CC/CV hybrid output and ZPA operation are mainly developed based on conventional two-coil WPT structures. However, conventional two-coil WPT systems suffer from engineering limitations, such as short transmission distances and limited degrees of freedom for parameter tuning. To improve the transmission distance and increase the degrees of freedom for parameter tuning, one or more repeater coils are commonly inserted between the transmitter and receiver coils, resulting in the formation of three-coil or multi-coil resonant compensation topologies.

Compared with conventional two-coil WPT systems, multi-coil WPT systems exhibit more complex and diverse resonant conditions, making it more challenging to achieve CC/CV hybrid output and ZPA operation. In [23–25], multi-relay architectures (domino coils) are employed to effectively enhance the transmission distance and improve the efficiency at specific operating points. However, the parameter tuning of these approaches relies on static load conditions. Consequently, under the dynamic load variations in WPT systems, they are unable to achieve CC/CV hybrid charging and maintain ZPA characteristics simultaneously. In [26–29], high-order compensation networks are introduced to improve the output characteristics under specific operating conditions. Nevertheless, limited by the fixed resonant network parameters, these approaches can only achieve a single CC or CV output characteristic. Furthermore, during CC-to-CV mode transitions under wide load variations, the system becomes detuned, resulting in the degradation of ZPA performance. In [30–34], auxiliary AC switches or relay arrays are introduced to dynamically reconfigure the compensation topology, thereby achieving CC/CV hybrid charging and ZPA operation. However, similar to the topology reconstruction method mentioned above, these hard-switching mechanisms require complex switching logic, which considerably increases the control complexity of WPT systems.

To address the aforementioned limitations of WPT systems, this paper proposes a dual-frequency compatible LCC-S-S and S-S-S compensated three-coil topology with CC and CV outputs for WPT applications, along with its parameter tuning method. The resonance conditions and ZPA operating conditions are systematically derived. The proposed compensation topology requires neither modification of the inherent system parameters nor additional relays or complicated control strategies. By simply switching between two resonant frequencies, the proposed topology realizes dual-mode CC/CV operation while simultaneously maintaining the ZPA input characteristics.

Specifically, the core innovations of the proposed method over previous studies are listed as follows:

(1) Based on the research background of three-coil compensated WPT topologies, this paper proposes a dual-frequency compatible topology. Without modifying the inherent system parameters or introducing additional complex control strategies and hardware components, the proposed topology achieves load-independent CC/CV output characteristics and ZPA operation at both resonant frequencies, thereby reducing the overall system cost and control complexity.

(2) Based on the proposed three-coil compensated topology, a parameter design method is developed. The proposed method enables the ZPA operation characteristics of both operating modes to be insensitive to variations in the coil coupling coefficient. Consequently, no parameter redesign is required under different coupling conditions, and stable ZPA operation can be maintained at both resonant frequencies, significantly enhancing the robustness and adaptability of the system.

2. Theoretical Analysis of the Proposed Compensation Topology

The proposed compensation topology is shown in Figure 2. The proposed three-coil compensation topology mainly consists of a DC voltage source U_{dc}, a high-frequency inverter (HFI), a three-coil coupler, three resonant compensation networks, a single-phase bridge rectifier (SBR), and a battery load. The full-bridge HFI is composed of four power MOSFETs (Q_1–Q_4) and is used to convert the DC voltage U_{dc} into the high-frequency AC voltage $\dot{U}_{\mathrm{AB}}$.

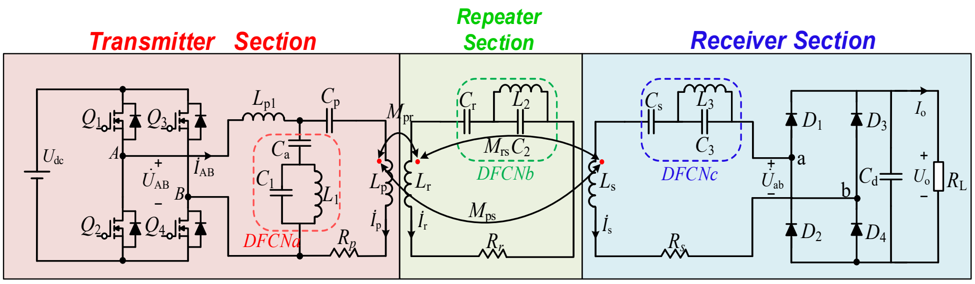

Figure 2. Dual-frequency switchable LCC-S-S and S-S-S compensated three-coil topology.

The duty cycle of the aforementioned square-wave voltage $\dot{U}_{\mathrm{AB}}$ is set to 0.5. For simplicity of analysis, the fundamental harmonic analysis (FHA) method is adopted to analyze this voltage waveform. Under this condition, the root mean square (RMS) amplitude of the first harmonic for the square-wave voltage $\dot{U}_{\mathrm{AB}}$ is formulated as:

$$U_{\mathrm{AB}} = \left|\dot{U}_{\mathrm{AB}}\right| \frac{2\sqrt{2}}{\pi} U_{\mathrm{dc}} \tag{1}$$

The three-coil coupler consists of a transmitter coil, a repeater coil, and a receiver coil. The respective self-inductances are defined as L_{p}, L_{r}, and L_{s}. The magnetic couplings among the coils are quantified by the mutual inductances M_{pr}, M_{ps}, and M_{rs}, respectively, and R_{p}, R_{r}, and R_{s} represent the parasitic resistances of the three coils.

The transmitter-side resonant compensation network consists of two compensation inductors L_{p1} and L_1 and three compensation capacitors C_{a}, C_{p}, and C_1. The repeater-side compensation network consists of one compensation inductor L_2 and two compensation capacitors C_{r} and C_2. The receiver-side compensation network consists of one compensation inductor L_3 and two compensation capacitors C_s and C_3. The transmitter, repeater, and receiver sides are each equipped with a dual-frequency compensation network (DFCN), namely DFCNa, DFCNb, and DFCNc, respectively. The operating mechanism and parameter design procedure of the DFCNs will be presented in detail in the subsequent sections.

The SBR is composed of four diodes (D_1–D_4) and is used to convert the AC voltage $\dot{U}_{ab}$ and AC current $\dot{I}_s$ into DC output voltage and current. The corresponding rectified voltage and current are denoted as U_o and I_o, respectively. With the output low-pass filter composed of a DC capacitor C_d, the RMS values of the AC and DC components satisfy the following relationship:

$$\begin{cases} U_o = \frac{\pi\sqrt{2}}{4}\dot{U}_{ab} \\ I_o = \frac{2\sqrt{2}}{\pi}\dot{I}_s \end{cases} \tag{2}$$

In Equation (2), let $\dot{U}_{ab}$ and $\dot{I}_s$ represent the RMS values for the AC input voltage and current of the full-bridge rectifier. Based on (2), the relationship between the equivalent AC resistance R_o and the battery's equivalent resistance can be expressed as:

$$R_o = \frac{8}{\pi^2}R_L \tag{3}$$

The general structure of the three DFCNs in Figure 2 is shown in Figure 3.

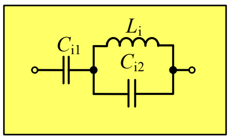

Figure 3. Schematic diagram of the DFCN structure.

The equivalent impedance Z_{DFCN} of the overall DFCN can be derived as follows:

$$\begin{aligned} Z_{DFCN} &= \frac{1}{j\omega C_{i1}} + \frac{1}{1/j\omega L_i + j\omega C_{i2}} \\ &= \frac{j\left[\omega^2 L_i (C_{i1}+C_{i2})-1\right]}{\omega C_{i1}(1-\omega^2 L_i C_{i2})} \end{aligned} \tag{4}$$

It can be observed from (4) that the DFCN exhibits different resonance characteristics under different operating frequencies ω. The resonance conditions and characteristics of the DFCN at different operating frequencies are listed in Table 1. In Table 1, ω_{sc} and ω_{oc} denote the operating frequencies at which the DFCN exhibits short-circuit and open-circuit characteristics, respectively.

Table 1. Characteristics of the DFCN.

Mode	**I**	**II**	**III**	**IV**
DFCN equivalent model	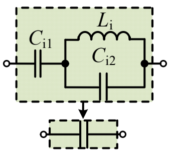	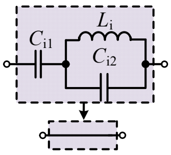	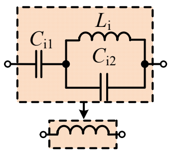	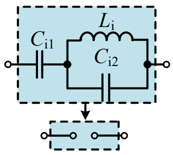
Resonant condition	$0 < \omega < \omega_{sc}$, $\omega > \omega_{oc}$	$\omega = \omega_{sc} = 1/\sqrt{L_i(C_{i1}+C_{i2})}$	$\omega_{sc} < \omega < \omega_{oc}$	$\omega = \omega_{oc} = 1/\sqrt{L_i C_{i2}}$
Impedance characteristics	$-jx(x>0)$ Capacitive	0 Short circuit	$+jx(x>0)$ Inductive	∞ Open circuit

https://doi.org/10.3390/electronics15184285

For simplicity of subsequent analysis, the HFI and SBR in Figure 2 can be equivalently modeled as a sinusoidal voltage source $\dot{U}_{ab}$ and an AC equivalent resistance R_o, respectively, according to (1) and (3). Meanwhile, the three DFCNs in Figure 2 can be equivalently modeled as three general reactances $Z_i = j\omega X_i$ (i = a, b, c), respectively. Considering the large separation distance between the transmitter and receiver coils, the mutual inductance M_{ps} between them and the parasitic resistances R_p, R_r, and R_s of the coils are neglected. Accordingly, the proposed compensation topology in Figure 2 is simplified into an equivalent circuit based on the mutual inductance model, as shown in Figure 4.

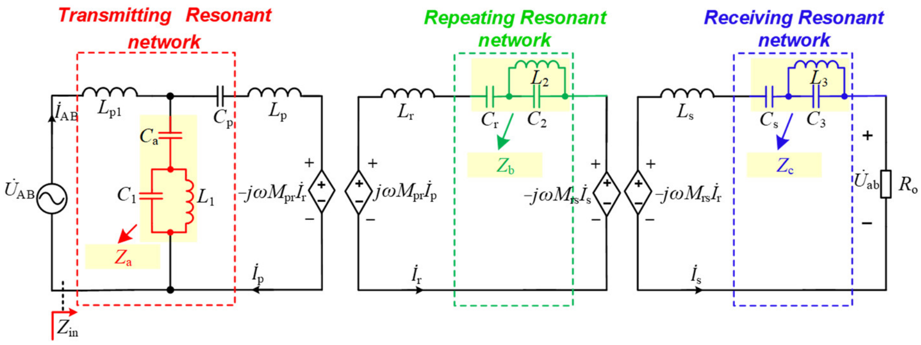

Figure 4. Equivalent circuit model of the proposed compensation topology.

When the system is tuned to the resonant frequency ω_{CC}, all three DFCNs in the proposed compensation topology are operated under Mode I conditions given in Table 1, and they can be equivalently represented as three resonant compensation capacitors C_{xa}, C_{xb}, and C_{xc}. Under this condition, the proposed compensation topology can be equivalently transformed into an LCC-S-S structure, and its corresponding equivalent circuit is illustrated in Figure 5.

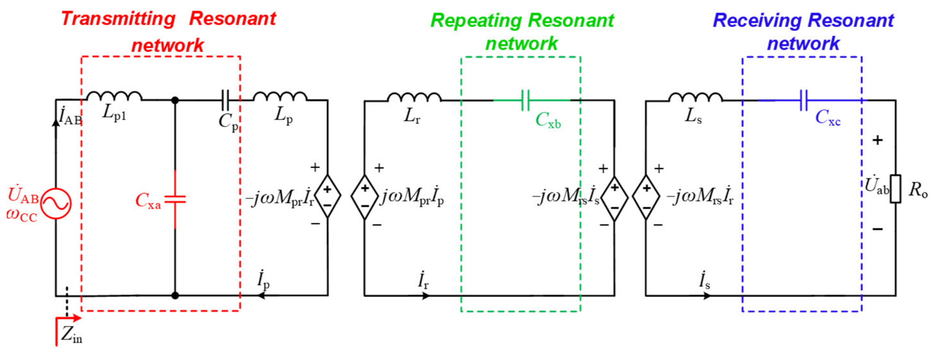

Figure 5. Equivalent LCC-S-S structure of the proposed compensation topology in CC mode.

The expressions of the three equivalent resonant compensation capacitors C_{xa}, C_{xb}, and C_{xc} are given as follows:

$$\begin{cases} C_{xa} = \frac{C_a(\omega^2 L_1 C_1 - 1)}{\omega^2 L_1 (C_1 + C_a) - 1} \\ C_{xb} = \frac{C_r(\omega^2 L_2 C_2 - 1)}{\omega^2 L_2 (C_2 + C_r) - 1} \\ C_{xc} = \frac{C_s(\omega^2 L_3 C_3 - 1)}{\omega^2 L_3 (C_3 + C_s) - 1} \end{cases} \quad (5)$$

The equivalent circuit of the designed topology is established based on the mutual inductance model, as depicted in Figure 5. According to this figure, the voltage equations of each loop can be established according to Kirchhoff's voltage law (KVL), as expressed in (6).

$$\begin{bmatrix} \dot{U}_{\mathrm{AB}} \\ 0 \\ 0 \\ 0 \end{bmatrix} = \begin{bmatrix} j\omega L_{\mathrm{p1}} + (j\omega C_{\mathrm{xa}})^{-1} & (j\omega C_{\mathrm{xa}})^{-1} & 0 & 0 \\ (j\omega C_{\mathrm{xa}})^{-1} & j\omega L_{\mathrm{p}} + (j\omega C_{\mathrm{p}})^{-1} + (j\omega C_{\mathrm{xa}})^{-1} & j\omega M_{\mathrm{pr}} & 0 \\ 0 & j\omega M_{\mathrm{pr}} & j\omega L_{\mathrm{r}} + (j\omega C_{\mathrm{xb}})^{-1} & j\omega M_{\mathrm{rs}} \\ 0 & 0 & j\omega M_{\mathrm{rs}} & j\omega L_{\mathrm{s}} + (j\omega C_{\mathrm{xc}})^{-1} + R_{\mathrm{o}} \end{bmatrix} \begin{bmatrix} \dot{I}_{\mathrm{AB}} \\ \dot{I}_{\mathrm{p}} \\ \dot{I}_{\mathrm{r}} \\ \dot{I}_{\mathrm{s}} \end{bmatrix} \tag{6}$$

where $\dot{I}_{\mathrm{AB}}$, $\dot{I}_{\mathrm{p}}$, $\dot{I}_{\mathrm{r}}$, and $\dot{I}_{\mathrm{s}}$ denote the loop currents, respectively. To facilitate the subsequent theoretical derivation, the impedance terms in the KVL matrix of (6) are simplified as follows:

$$\begin{cases} Z_{\mathrm{a\_CC}} = (j\omega C_{\mathrm{xa}})^{-1} \\ Z_{\mathrm{b\_CC}} = (j\omega C_{\mathrm{xb}})^{-1} \\ Z_{\mathrm{c\_CC}} = (j\omega C_{\mathrm{xc}})^{-1} \\ Z_{\mathrm{1\_CC}} = j\omega L_{\mathrm{p1}} + Z_{\mathrm{a\_CC}} \\ Z_{\mathrm{2\_CC}} = j\omega L_{\mathrm{p}} + (j\omega C_{\mathrm{p}})^{-1} + Z_{\mathrm{a\_CC}} \\ Z_{\mathrm{3\_CC}} = j\omega L_{\mathrm{r}} + Z_{\mathrm{b\_CC}} \\ Z_{\mathrm{4\_CC}} = j\omega L_{\mathrm{s}} + Z_{\mathrm{c\_CC}} \end{cases} \tag{7}$$

The mutual inductance terms can be equivalently expressed as:

$$\begin{cases} Z_{\mathrm{Mpr}} = j\omega M_{\mathrm{pr}} \\ Z_{\mathrm{Mrs}} = j\omega M_{\mathrm{rs}} \end{cases} \tag{8}$$

Combining (6)–(8), the loop KVL matrix can be simplified as follows:

$$\begin{cases} \dot{U}_{\mathrm{AB}} = Z_{\mathrm{1\_CC}}\dot{I}_{\mathrm{AB}} - Z_{\mathrm{a\_CC}}\dot{I}_{\mathrm{p}} \\ 0 = -Z_{\mathrm{a\_CC}}\dot{I}_{\mathrm{AB}} + Z_{\mathrm{2\_CC}}\dot{I}_{\mathrm{p}} - Z_{\mathrm{Mpr}}\dot{I}_{\mathrm{r}} \\ 0 = Z_{\mathrm{Mpr}}\dot{I}_{\mathrm{p}} - Z_{\mathrm{3\_CC}}\dot{I}_{\mathrm{r}} + Z_{\mathrm{Mrs}}\dot{I}_{\mathrm{s}} \\ 0 = -Z_{\mathrm{Mrs}}\dot{I}_{\mathrm{r}} + Z_{\mathrm{4\_CC}}\dot{I}_{\mathrm{s}} + R_{\mathrm{o}}\dot{I}_{\mathrm{s}} \end{cases} \tag{9}$$

Based on (9), the input AC current $\dot{I}_{\mathrm{AB}}$ and output AC current $\dot{I}_{\mathrm{s}}$ can be further derived as follows:

$$\begin{cases} \dot{I}_{\mathrm{AB}} = \dfrac{Z_{\mathrm{2\_CC}}Z_{\mathrm{Mrs}}^2 - Z_{\mathrm{2\_CC}}Z_{\mathrm{3\_CC}}Z_{\mathrm{4\_CC}} + Z_{\mathrm{4\_CC}}Z_{\mathrm{Mpr}}^2 + (Z_{\mathrm{Mpr}}^2 - Z_{\mathrm{2\_CC}}Z_{\mathrm{3\_CC}})R_{\mathrm{o}}}{\alpha_{\mathrm{CC}} + \beta_{\mathrm{CC}}R_{\mathrm{o}}}\dot{U}_{\mathrm{AB}} \\ \dot{I}_{\mathrm{s}} = \dfrac{Z_{\mathrm{a\_CC}}Z_{\mathrm{Mpr}}Z_{\mathrm{Mrs}}}{\alpha_{\mathrm{CC}} + \beta_{\mathrm{CC}}R_{\mathrm{o}}}\dot{U}_{\mathrm{AB}} \end{cases} \tag{10}$$

where α_{CC} and β_{CC} are defined as:

$$\begin{cases} \alpha_{\mathrm{CC}} = (Z_{\mathrm{1\_CC}}Z_{\mathrm{2\_CC}} - Z_{\mathrm{a\_CC}}^2)Z_{\mathrm{Mrs}}^2 + (Z_{\mathrm{Mpr}}^2 - Z_{\mathrm{2\_CC}}Z_{\mathrm{3\_CC}})Z_{\mathrm{1\_CC}}Z_{\mathrm{4\_CC}} + Z_{\mathrm{3\_CC}}Z_{\mathrm{4\_CC}}Z_{\mathrm{a\_CC}}^2 \\ \beta_{\mathrm{CC}} = Z_{\mathrm{1\_CC}}Z_{\mathrm{Mpr}}^2 + Z_{\mathrm{3\_CC}}Z_{\mathrm{a\_CC}}^2 - Z_{\mathrm{1\_CC}}Z_{\mathrm{2\_CC}}Z_{\mathrm{3\_CC}} \end{cases} \tag{11}$$

Based on (10), the analytical expressions of the transconductance gain G_{IV} and the input impedance $Z_{\mathrm{in\_CC}}$ under this mode can be further derived as follows:

$$G_{\mathrm{IV}} = \left| \frac{\dot{I}_{\mathrm{s}}}{\dot{U}_{\mathrm{AB}}} \right| = \left| \frac{Z_{\mathrm{a\_CC}}Z_{\mathrm{Mpr}}Z_{\mathrm{Mrs}}}{\alpha_{\mathrm{CC}} + \beta_{\mathrm{CC}}R_{\mathrm{o}}} \right| \tag{12}$$

$$Z_{\mathrm{in\_CC}} = \left| \frac{\dot{U}_{\mathrm{AB}}}{\dot{I}_{\mathrm{AB}}} \right| = \left| \frac{\alpha_{\mathrm{CC}} + \beta_{\mathrm{CC}}R_{\mathrm{o}}}{Z_{\mathrm{2\_CC}}Z_{\mathrm{Mrs}}^2 - Z_{\mathrm{2\_CC}}Z_{\mathrm{3\_CC}}Z_{\mathrm{4\_CC}} + Z_{\mathrm{4\_CC}}Z_{\mathrm{Mpr}}^2 + (Z_{\mathrm{Mpr}}^2 - Z_{\mathrm{2\_CC}}Z_{\mathrm{3\_CC}})R_{\mathrm{o}}} \right| \tag{13}$$

According to the transconductance gain expression in (12), a load-independent CC output can be achieved when $\beta_{\text{CC}} = 0$. The corresponding resonance condition is given as follows:

$$\beta_{\text{CC}} = Z_{1\_\text{CC}}Z_{\text{Mpr}}^2 + Z_{3\_\text{CC}}Z_{\text{a\_CC}}^2 - Z_{1\_\text{CC}}Z_{2\_\text{CC}}Z_{3\_\text{CC}} = 0 \tag{14}$$

According to (13), when $\beta_{\text{CC}} = 0$, the input impedance $Z_{\text{in\_CC}}$ should be purely resistive to ensure ZPA operation in the CC mode. Therefore, the following condition should be satisfied:

$$Z_{2\_\text{CC}}Z_{\text{Mrs}}^2 - Z_{2\_\text{CC}}Z_{3\_\text{CC}}Z_{4\_\text{CC}} + Z_{4\_\text{CC}}Z_{\text{Mpr}}^2 = 0 \tag{15}$$

Theoretically, there are an infinite number of solutions that satisfy Equation (15). Considering that the misalignment of the coupling mechanism during the actual charging process causes variations in the mutual inductance, to prevent the ZPA condition in the CC mode from being affected by the mutual inductances M_{rs} and M_{pr} during practical system operation, Z_{2_CC} and Z_{4_CC} in Equation (15) can be set to zero, yielding:

$$\omega_{\text{CC}}^2 = \frac{1}{L_{\text{p}}C_{\text{p}}} + \frac{1}{L_{\text{p}}C_{\text{xa}}} = \frac{1}{L_{\text{s}}C_{\text{xc}}} \tag{16}$$

Based on the above analysis, substituting $Z_{2\_\text{CC}} = 0$ into Equation (14) yields:

$$\beta_{\text{CC}} = Z_{1\_\text{CC}}Z_{\text{Mpr}}^2 + Z_{3\_\text{CC}}Z_{\text{a\_CC}}^2 = 0 \tag{17}$$

The solution sets satisfying Equation (17) can be divided into two cases: one is $Z_{1\_\text{CC}} = Z_{3\_\text{CC}} = 0$, and the other is $Z_{1\_\text{CC}} \neq 0$, $Z_{3\_\text{CC}} \neq 0$. Similarly, to prevent the CC output condition of the system from being affected by the mutual inductance M_{pr} during actual system operation, $Z_{1\_\text{CC}} = Z_{3\_\text{CC}} = 0$ should be selected as the solution for Equation (17). Combining this with Equation (7), the resonant conditions for achieving the CC output of the system can be obtained as:

$$\omega_{\text{CC}}^2 = \frac{1}{L_{\text{p1}}C_{\text{xa}}} = \frac{1}{L_{\text{r}}C_{\text{xb}}} \tag{18}$$

At the resonant frequency ω_1, the magnitude of the output AC current $\dot{I}_{\text{s}}$ can be expressed as:

$$\dot{I}_{\text{s}} = \frac{jM_{\text{pr}}\dot{U}_{\text{AB}}}{\omega_{\text{CC}}M_{\text{rs}}L_{\text{p1}}} \tag{19}$$

According to the relationship between the AC and DC currents before and after rectification, the expression for the DC output current I_{o} can be obtained as:

$$I_{\text{o}} = \frac{8M_{\text{pr}}U_{\text{dc}}}{\pi^2\omega_{\text{CC}}M_{\text{rs}}L_{\text{p1}}} \tag{20}$$

When the system is tuned to the resonant frequency ω_{CV}, setting DFCNa in the compensation topology to operate under Mode IV as shown in Table 1 makes it equivalent to an open circuit; simultaneously, setting DFCNb and DFCNc to operate under Mode I as shown in Table 1 makes them equivalent to two capacitors C_{xb} and C_{xc}. At this time, the proposed compensation topology can be equivalent to an S-S-S structure, and its equivalent circuit is shown in Figure 6.

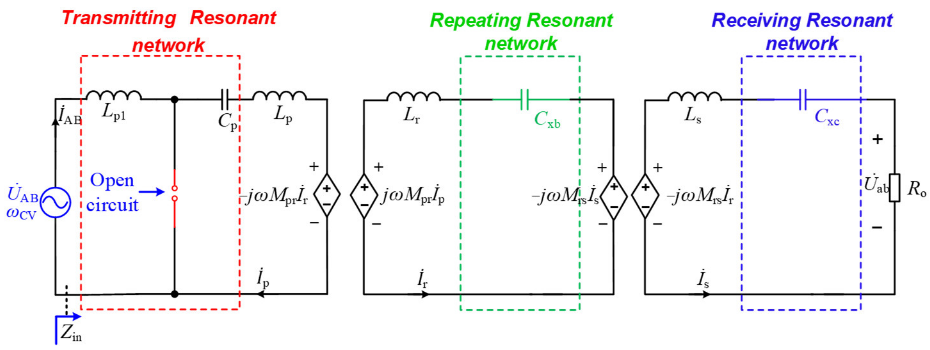

Figure 6. Equivalent S-S-S structure of the proposed compensation topology in CV mode.

In CV mode, since DNCNa is equivalent to an open circuit, parallel resonance occurs between L_1 and C_1 in DFCNa:

$$\omega_{\mathrm{CV}}^2 = \frac{1}{L_1 C_1} \tag{21}$$

Based on the equivalent circuit of the proposed compensation topology with the mutual inductance model shown in Figure 6, and applying KVL, the loop voltage equations can be formulated as shown in Equation (21):

$$\begin{bmatrix} \dot{U}_{\mathrm{AB}} \\ 0 \\ 0 \end{bmatrix} = \begin{bmatrix} j\omega L_{\mathrm{p1}} + (j\omega C_{\mathrm{p}})^{-1} + j\omega L_{\mathrm{p}} & j\omega M_{\mathrm{pr}} & 0 \\ j\omega M_{\mathrm{pr}} & j\omega L_{\mathrm{r}} + (j\omega C_{\mathrm{xb}})^{-1} & j\omega M_{\mathrm{rs}} \\ 0 & j\omega M_{\mathrm{rs}} & j\omega L_{\mathrm{s}} + (j\omega C_{\mathrm{xc}})^{-1} + R_{\mathrm{o}} \end{bmatrix} \begin{bmatrix} \dot{I}_{\mathrm{AB}} \\ \dot{I}_{\mathrm{r}} \\ \dot{I}_{\mathrm{s}} \end{bmatrix} \tag{22}$$

To facilitate subsequent theoretical derivations, the impedance terms in the KVL matrix corresponding to Equation (21) are appropriately simplified:

$$\begin{cases} Z_{\mathrm{b\_CV}} = (j\omega C_{\mathrm{xb}})^{-1} \\ Z_{\mathrm{c\_CV}} = (j\omega C_{\mathrm{xc}})^{-1} \\ Z_{1\_\mathrm{CV}} = j\omega L_{\mathrm{p1}} + (j\omega C_{\mathrm{p}})^{-1} + j\omega L_{\mathrm{p}} \\ Z_{2\_\mathrm{CV}} = j\omega L_{\mathrm{r}} + Z_{\mathrm{b\_CV}} \\ Z_{3\_\mathrm{CV}} = j\omega L_{\mathrm{s}} + Z_{\mathrm{c\_CV}} \end{cases} \tag{23}$$

By combining Equations (8), (22) and (23), the loop KVL matrix can be simplified to:

$$\begin{cases} \dot{U}_{\mathrm{AB}} = Z_{1\_\mathrm{CV}} \dot{I}_{\mathrm{AB}} - Z_{\mathrm{Mpr}} \dot{I}_{\mathrm{r}} \\ 0 = -Z_{\mathrm{Mpr}} \dot{I}_{\mathrm{AB}} + Z_{2\_\mathrm{CV}} \dot{I}_{\mathrm{r}} - Z_{\mathrm{Mrs}} \dot{I}_{\mathrm{s}} \\ 0 = -Z_{\mathrm{Mrs}} \dot{I}_{\mathrm{r}} + Z_{3\_\mathrm{CV}} \dot{I}_{\mathrm{s}} + R_{\mathrm{o}} \dot{I}_{\mathrm{s}} \end{cases} \tag{24}$$

Based on Equation (24), the current expressions for the input AC current $\dot{I}_{\mathrm{AB}}$ and the output AC current $\dot{I}_{\mathrm{s}}$ in CV mode can be further derived as:

$$\begin{cases} \dot{I}_{\mathrm{AB}} = \frac{Z_{2\_\mathrm{CV}} Z_{3\_\mathrm{CV}} - Z_{\mathrm{Mrs}}^2 + Z_{2\_\mathrm{CV}} R_{\mathrm{o}}}{\alpha_{\mathrm{CV}} + \beta_{\mathrm{CV}} R_{\mathrm{o}}} \dot{U}_{\mathrm{AB}} \\ \dot{I}_{\mathrm{s}} = \frac{Z_{\mathrm{Mpr}} Z_{\mathrm{Mrs}}}{\alpha_{\mathrm{CV}} + \beta_{\mathrm{CV}} R_{\mathrm{o}}} \dot{U}_{\mathrm{AB}} \end{cases} \tag{25}$$

where α_{CV} and β_{CV} are expressed as:

$$\begin{cases} \alpha_{\mathrm{CV}} = Z_{1\_\mathrm{CV}} Z_{2\_\mathrm{CV}} Z_{3\_\mathrm{CV}} - Z_{1\_\mathrm{CV}} Z_{\mathrm{Mrs}}^2 + Z_{\mathrm{Mpr}}^2 Z_{3\_\mathrm{CV}} \\ \beta_{\mathrm{CV}} = Z_{1\_\mathrm{CV}} Z_{2\_\mathrm{CV}} - Z_{\mathrm{Mpr}}^2 \end{cases} \tag{26}$$

Based on Equation (25), the analytical expressions for the voltage gain G_{VV} and the input impedance $Z_{\mathrm{in\_CV}}$ are as follows:

$$G_{\mathrm{VV}} = \left|\frac{\dot{I}_{\mathrm{s}}R_{\mathrm{o}}}{\dot{U}_{\mathrm{AB}}}\right| = \left|\frac{Z_{\mathrm{Mpr}}Z_{\mathrm{Mrs}}}{\alpha_{\mathrm{CV}}R_{\mathrm{o}}^{-1} + \beta_{\mathrm{CV}}}\right| \tag{27}$$

$$Z_{\mathrm{in\_CV}} = \left|\frac{\dot{U}_{\mathrm{AB}}}{\dot{I}_{\mathrm{AB}}}\right| = \left|\frac{\alpha_{\mathrm{CV}} + \beta_{\mathrm{CV}}R_{\mathrm{o}}}{Z_{2\_\mathrm{CV}}Z_{3\_\mathrm{CV}} - Z_{\mathrm{Mrs}}^{2} + Z_{2\_\mathrm{CV}}R_{\mathrm{o}}}\right| \tag{28}$$

According to the voltage gain Equation (27), when the parameter $\alpha_{\mathrm{CV}} = 0$, a load-independent CV output can be realized by the proposed system, and the corresponding resonant condition is given as:

$$\alpha_{\mathrm{CV}} = Z_{1\_\mathrm{CV}}Z_{2\_\mathrm{CV}}Z_{3\_\mathrm{CV}} - Z_{1\_\mathrm{CV}}Z_{\mathrm{Mrs}}^{2} + Z_{\mathrm{Mpr}}^{2}Z_{3\_\mathrm{CV}} = 0 \tag{29}$$

According to Equation (28), when $\alpha_{\mathrm{CV}} = 0$, in order to make the input impedance $Z_{\mathrm{in\_CV}}$ purely resistive and ensure ZPA operation in CV mode, the following condition must be satisfied:

$$Z_{2\_\mathrm{CV}} = 0 \tag{30}$$

Namely, the ZPA realization condition in CV mode is:

$$\omega_{\mathrm{CV}}^{2} = \frac{1}{L_{\mathrm{r}}C_{\mathrm{xb}}} \tag{31}$$

Substituting $Z_{2\_\mathrm{CV}} = 0$ into Equation (29) yields:

$$\alpha_{\mathrm{CV}} = -Z_{1\_\mathrm{CV}}Z_{\mathrm{Mrs}}^{2} + Z_{\mathrm{Mpr}}^{2}Z_{3\_\mathrm{CV}} = 0 \tag{32}$$

The solution sets satisfying Equation (32) can be divided into two cases: one is $Z_{1\_\mathrm{CV}} = Z_{3\_\mathrm{CV}} = 0$, and the other is $Z_{1\_\mathrm{CV}} \neq 0$, $Z_{3\_\mathrm{CV}} \neq 0$. Similarly, to prevent the CV output condition of the system from being affected by the mutual inductance M_{pr} and M_{rs} during actual system operation, $Z_{1\_\mathrm{CV}} = Z_{3\_\mathrm{CV}} = 0$ should be selected as the solution for Equation (32). Combining this with Equation (23), the resonant conditions for achieving the CV output of the system can be obtained as:

$$\omega_{\mathrm{CV}}^{2} = \frac{1}{(L_{\mathrm{p1}} + L_{\mathrm{p}})C_{\mathrm{p}}} = \frac{1}{L_{\mathrm{s}}C_{\mathrm{xc}}} \tag{33}$$

At the resonant frequency ω_{CV}, the magnitude of the output AC voltage $\dot{U}_{\mathrm{ab}}$ can be expressed as:

$$\dot{U}_{\mathrm{ab}} = \frac{M_{\mathrm{rs}}\dot{U}_{\mathrm{AB}}}{M_{\mathrm{pr}}} \tag{34}$$

According to the relationship between AC and DC voltages before and after rectification, the expression for the DC output voltage U_{o} can be obtained as:

$$\dot{U}_{\mathrm{o}} = \frac{M_{\mathrm{rs}}\dot{U}_{\mathrm{dc}}}{M_{\mathrm{pr}}} \tag{35}$$

3. Design Procedure of System Parameters and Controller

The compensation topology parameters are critical factors for the WPT system to achieve CC/CV frequency switching. To realize hybrid CC/CV wireless charging and ZPA operation of the input impedance, the component parameters of the proposed dual-frequency compatible WPT system need to be designed based on the aforementioned resonant conditions in CC and CV modes. The parameter design method for achieving CC/CV output and ZPA operation of the system is detailed below.

First, according to the specific requirements of the application, certain parameters of the proposed dual-frequency compatible compensation topology are preset, as shown in Table 2. To determine the remaining resonant parameters of the compensation topology, a comprehensive analysis must be performed by combining the resonant conditions for CC/CV output and ZPA operation derived in Section 2.

Table 2. Preset parameters of the proposed dual-frequency switchable compensation topology.

Symbols	Parameters	Values
U_{dc}	DC-link input voltage	200 V
f_{CC}	Resonant frequency1 (for CC mode)	200 kHz
f_{CV}	Resonant frequency2 (for CV mode)	85 kHz
P_o	Output power rating	400 W
U_o	Charging voltage	80 V
I_o	Charging current	5 A
L_r	Repeating coil inductance	308 µH
L_s	Receiving coil inductance	210 µH
L_i	Parallel compensation inductance of DFCN	100 µH
M_{pr}	Transmitting and repeating mutual inductance	65 µH

First, based on the preset constant DC output voltage in Table 2 and Equation (35), the mutual inductance M_{rs} between the repeater coil and the receiver coil in the system can be calculated as:

$$M_{rs} = \frac{M_{pr}U_o}{U_{dc}} \tag{36}$$

According to the preset constant DC output current in Table 2 and Equation (20), the value of the transmitter side series compensation inductor L_{p1} can be calculated as:

$$L_{p1} = \frac{8M_{pr}U_{dc}}{\pi^2\omega_{CC}M_{rs}I_o} \tag{37}$$

According to the system CV resonant condition shown in Equation (21), the value of the parallel resonant compensation capacitor C_1 in DFCNa can be calculated as:

$$C_1 = \frac{1}{\omega_{CV}^2 L_1} \tag{38}$$

According to the system CC resonant condition shown in Equation (18), and by simultaneously solving Equations (5) and (18), the value of the series resonant compensation capacitor C_a in DFCNa can be calculated as

$$C_a = \frac{1-\omega_{CC}^2 L_1 C_1}{\omega_{CC}^2 (L_1 + L_{p1} - \omega_{CC}^2 L_{p1} L_1 C_1)} \tag{39}$$

According to the CC and ZPA resonant conditions in CC mode shown in Equations (16) and (18), simultaneously solving Equations (16) and (18) yields:

$$\omega_{\mathrm{CC}}^2 = \frac{1}{(L_{\mathrm{p}} - L_{\mathrm{p1}})C_{\mathrm{p}}} \tag{40}$$

According to the system CV resonant condition shown in Equation (33), and by simultaneously solving Equations (33) and (41), the self-inductance L_{p} of the transmitter coil and the series compensation capacitor C_{p} can be obtained as:

$$\begin{cases} L_{\mathrm{p}} = \frac{L_{\mathrm{p1}}(\omega_{\mathrm{CC}}^2+\omega_{\mathrm{CV}}^2)}{\omega_{\mathrm{CC}}^2-\omega_{\mathrm{CV}}^2} \\ C_{\mathrm{p}} = \frac{\omega_{\mathrm{CC}}^2-\omega_{\mathrm{CV}}^2}{2L_{\mathrm{p1}}\omega_{\mathrm{CC}}^2\omega_{\mathrm{CV}}^2} \end{cases} \tag{41}$$

To achieve CC/CV output and ZPA operation over the entire load range for the proposed WPT system, Equations (5), (16), (18), (31) and (33) should be solved simultaneously to satisfy the resonant conditions for both CC/CV output and ZPA operation. Thus, two sets of solutions for capacitors C_{r}, C_2, C_{s} and C_3 can be obtained, denoted as $C_{\mathrm{r\_i}}$, C_{2_i}, $C_{\mathrm{s\_i}}$, C_{3_i} (i = 1, 2), respectively. The specific expressions for these two sets of capacitor parameters are as follows:

$$\begin{cases} C_{\mathrm{r\_i}} = \frac{\sqrt{L_{\mathrm{r}}}(\omega_{\mathrm{CC}}^2+\omega_{\mathrm{CV}}^2)\pm A}{2\sqrt{L_{\mathrm{r}}}\omega_{\mathrm{CC}}^2\omega_{\mathrm{CV}}^2(L_2+L_{\mathrm{r}})} \\ C_{2\_\mathrm{i}} = \frac{-L_2\sqrt{L_{\mathrm{r}}}\omega_{\mathrm{CC}}^2+L_2\sqrt{L_{\mathrm{r}}}\omega_{\mathrm{CV}}^2\mp(L_2+L_{\mathrm{r}})A-L_{\mathrm{r}}^{3/2}\omega_{\mathrm{CC}}^2+L_{\mathrm{r}}^{3/2}\omega_{\mathrm{CV}}^2}{L_2\omega_{\mathrm{CC}}^2\left(2L_2\sqrt{L_{\mathrm{r}}}\omega_{\mathrm{CV}}^2-L_{\mathrm{r}}^{3/2}\omega_{\mathrm{CC}}^2+L_{\mathrm{r}}^{3/2}\omega_{\mathrm{CV}}^2\mp L_{\mathrm{r}}A\right)} \\ C_{\mathrm{s\_i}} = \frac{\sqrt{L_{\mathrm{s}}}\omega_{\mathrm{CC}}^2+\sqrt{L_{\mathrm{s}}}\omega_{\mathrm{CV}}^2\pm B}{2\sqrt{L_{\mathrm{s}}}\omega_{\mathrm{CC}}^2\omega_{\mathrm{CV}}^2(L_3+L_{\mathrm{s}})} \\ C_{3\_\mathrm{i}} = \frac{-L_3\sqrt{L_{\mathrm{s}}}\omega_{\mathrm{CC}}^2+L_3\sqrt{L_{\mathrm{s}}}\omega_{\mathrm{CV}}^2\mp(L_3+L_{\mathrm{s}})B-L_{\mathrm{s}}^{3/2}\omega_{\mathrm{CC}}^2+L_{\mathrm{s}}^{3/2}\omega_{\mathrm{CV}}^2}{L_3\omega_{\mathrm{CC}}^2\left(2L_3\sqrt{L_{\mathrm{s}}}\omega_{\mathrm{CV}}^2-L_{\mathrm{s}}^{3/2}\omega_{\mathrm{CC}}^2+L_{\mathrm{s}}^{3/2}\omega_{\mathrm{CV}}^2\mp L_{\mathrm{s}}B\right)} \end{cases} \quad (\mathrm{i}=1,2) \tag{42}$$

where A and B are given by:

$$\begin{cases} A = \sqrt{-4L_2\omega_{\mathrm{CC}}^2\omega_{\mathrm{CV}}^2 + L_{\mathrm{r}}\omega_{\mathrm{CC}}^4 - 2L_{\mathrm{r}}\omega_{\mathrm{CC}}^2\omega_{\mathrm{CV}}^2 + L_{\mathrm{r}}\omega_{\mathrm{CV}}^4} \\ B = \sqrt{-4L_3\omega_{\mathrm{CC}}^2\omega_{\mathrm{CV}}^2 + L_{\mathrm{s}}\omega_{\mathrm{CC}}^4 - 2L_{\mathrm{s}}\omega_{\mathrm{CC}}^2\omega_{\mathrm{CV}}^2 + L_{\mathrm{s}}\omega_{\mathrm{CV}}^4} \end{cases} \tag{43}$$

Based on Equations (37)–(43) and the preset parameters of the proposed compensation topology listed in Table 2, the remaining resonant parameters of the proposed dual-frequency compatible compensation topology can be further calculated, as listed in Table 3:

As shown in Equations (42) and (43), the two DFCN in the repeater circuit and receiver circuit correspond to two different sets of resonant capacitance parameters. Although both sets of resonant parameters satisfy the system's CC/CV and ZPA resonant conditions, the system characteristics vary under different parameters. Therefore, it is necessary to perform a comparative analysis of the system performance under these two parameter sets to ultimately determine an optimal solution.

The definition of the system's input impedance angle θ_{in} is shown in Equation (44), where the operators "Im" and "Re" denote the imaginary and real parts of the input impedance, respectively:

$$\theta_{\mathrm{in}} = \frac{180^\circ}{\pi}\tan^{-1}\frac{\mathrm{Im}(\mathrm{Z_{in}})}{\mathrm{Re}(\mathrm{Z_{in}})} \tag{44}$$

Based on the compensation topology parameters given in Tables 2 and 3, along with Equations (12), (13), (27) and (28), the transconductance gain, voltage gain, and input phase angle of the system under two sets of different resonant compensation capacitor parameters were calculated and analyzed. Figure 7 shows the system frequency characteristic curves under these two sets of resonant parameters.

Table 3. Main resonant parameters of the proposed dual-frequency compensation topology.

Symbols	Parameters	Values
M_{rs}	Repeating and receiving mutual inductance	26 µH
L_{p1}	Transmitting compensation inductance	64.5 µH
C_1	Transmitting parallel compensation capacitance	35.06 nF
C_a	Transmitting series compensation capacitance	14.91 nF
L_p	Transmitting coil inductance	92.9 µH
C_p	Transmitting series compensation capacitance	22.26 nF
C_{r_1}	Repeating series compensation capacitance 1	7.91 nF
C_{2_1}	Repeating parallel compensation capacitance 1	9.11 nF
C_{s_1}	Receiving series compensation capacitance 1	9.91 nF
C_{3_1}	Receiving parallel compensation capacitance 1	10.67 nF
C_{r_2}	Repeating series compensation capacitance 2	2.23 nF
C_{2_2}	Repeating parallel compensation capacitance 2	32.28 nF
C_{s_2}	Receiving series compensation capacitance 2	3.44 nF
C_{3_2}	Receiving parallel compensation capacitance 2	30.73 nF

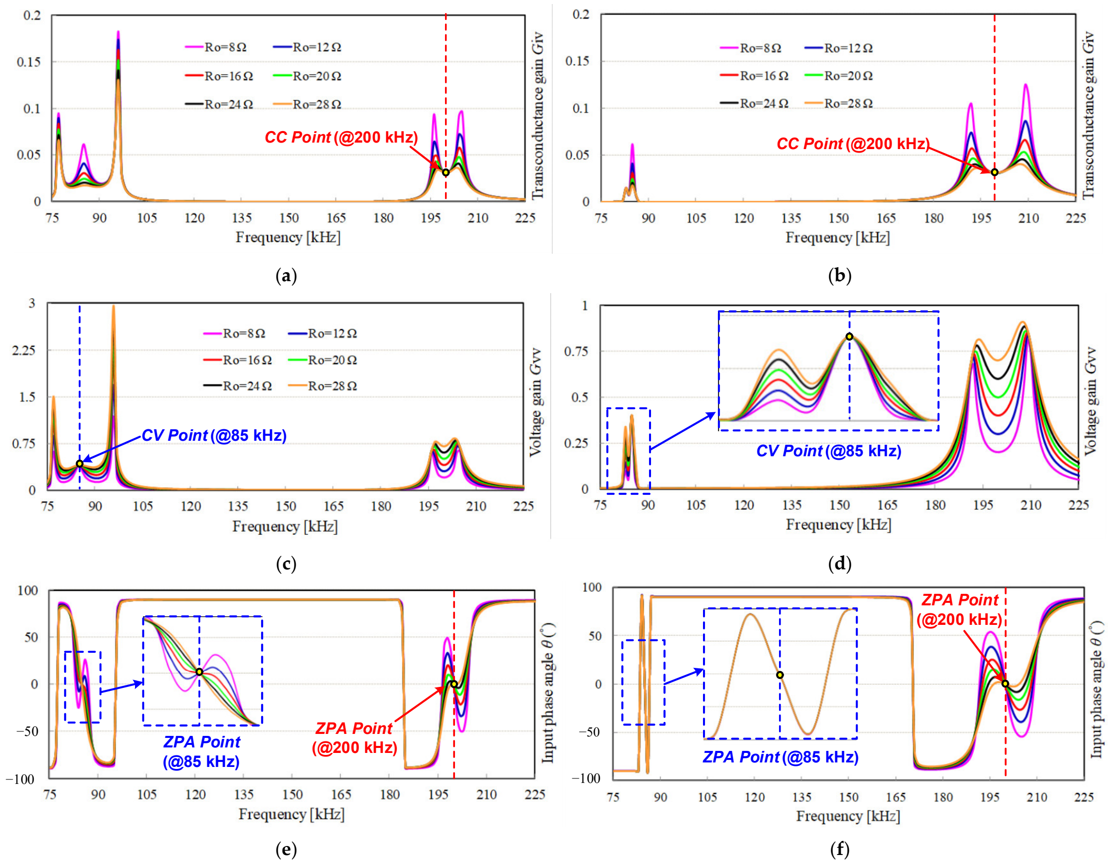

Figure 7. Transconductance gain, voltage gain, and input phase angle of the proposed compensation topology. (**a**) Transconductance gain (C_{r_1}, C_{2_1}, C_{s_1}, C_{3_1}). (**b**) Transconductance gain (C_{r_2}, C_{2_2}, C_{s_2}, C_{3_2}). (**c**) Voltage gain (C_{r_1}, C_{2_1}, C_{s_1}, C_{3_1}). (**d**) Voltage gain (C_{r_2}, C_{2_2}, C_{s_2}, C_{3_2}). (**e**) Input

phase angle (C_{r_1}, C_{2_1}, C_{s_1}, C_{3_1}). (**f**) Input phase angle (C_{r_2}, C_{2_2}, C_{s_2}, C_{3_2}). Furthermore, based on frequency response analysis, considering that system parameter design tolerances may vary across different resonance parameter sets, we also perform a sensitivity analysis of the system parameters under both resonance conditions to identify the more robust set of resonance parameters. The system phase angle, output voltage, and output current were calculated and plotted as functions of the nominal value under two distinct sets of capacitor parameters, as shown in Figure 8.

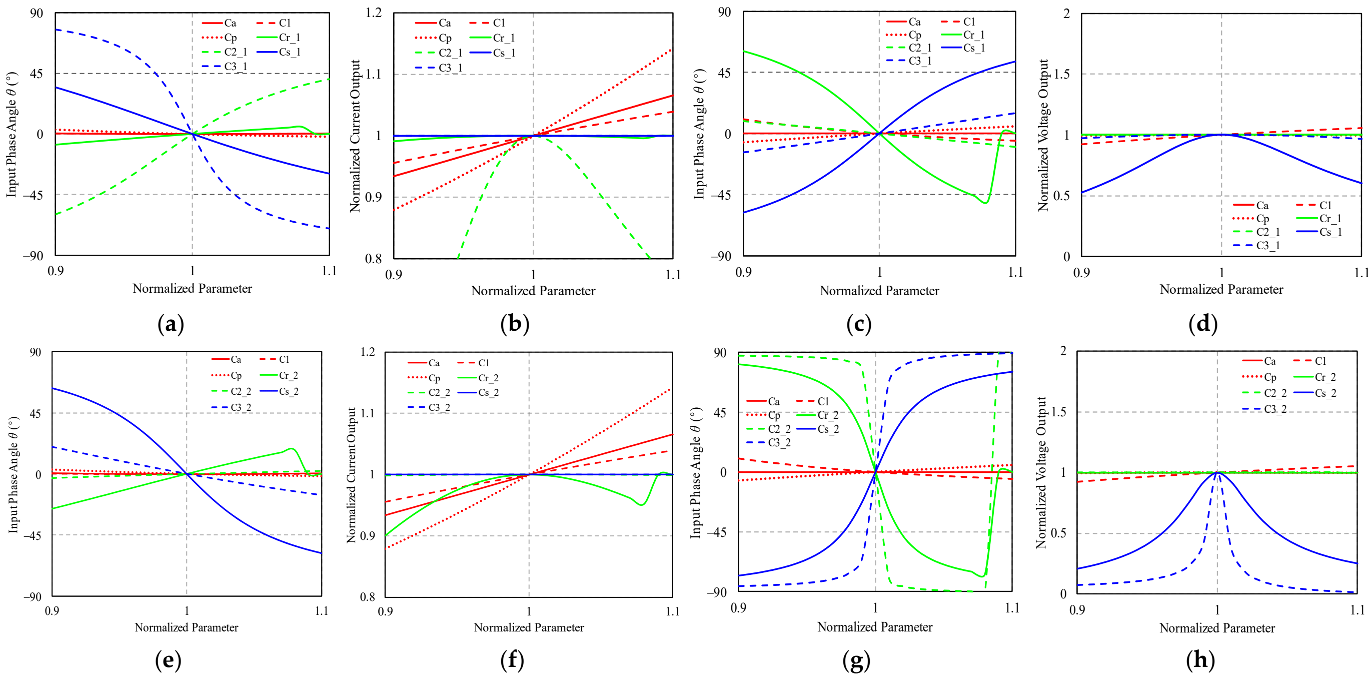

Figure 8. Input phase angle, normalized output current and voltage versus normalized resonant parameters under two sets of resonant parameters (@R_o = 16 Ω). (**a**) Input phase angle in CC mode (C_{r_1}, C_{2_1}, C_{s_1}, C_{3_1}). (**b**) Normalized output current in CC mode (C_{r_1}, C_{2_1}, C_{s_1}, C_{3_1}). (**c**) Input phase angle in CV mode (C_{r_1}, C_{2_1}, C_{s_1}, C_{3_1}). (**d**) Normalized output voltage in CV mode (C_{r_1}, C_{2_1}, C_{s_1}, C_{3_1}). (**e**) Input phase angle in CC mode (C_{r_2}, C_{2_2}, C_{s_2}, C_{3_2}). (**f**) Normalized output current in CC mode (C_{r_2}, C_{2_2}, C_{s_2}, C_{3_2}). (**g**) Input phase angle in CV mode (C_{r_2}, C_{2_2}, C_{s_2}, C_{3_2}). (**h**) Normalized output voltage in CV mode (C_{r_2}, C_{2_2}, C_{s_2}, C_{3_2}).

As can be seen from Figure 7a,b, over a wide load variation range, the system under both sets of resonant parameters achieves load-independent CC output at the resonant point ω_{CC} = 200 kHz. Furthermore, the transconductance gain G_{IV} of the system exhibits a non-monotonic variation on both sides of the CC resonant point, first increasing and then decreasing.

As can be seen from Figure 7c,d, under load variations, the system under both sets of resonant parameters achieves load-independent CV output at the resonant point ω_{CV} = 85 kHz. However, under the second set of resonant parameters, the system's voltage gain G_{VV} exhibits a monotonic decreasing trend on both sides of the CV resonant point, which is extremely sensitive to frequency offsets. This characteristic degrades the parameter tuning tolerance of the system.

As can be seen from Figure 7e,f, during variable load operation, the system under both sets of resonant parameters achieves ZPA operation at the resonant points ω_{CV} = 85 kHz and ω_{CC} = 200 kHz. However, under the second set of resonant parameters, the system's input impedance angle θ_{in} is likewise extremely sensitive to frequency offsets around 85 kHz. Specifically, when the system's operating frequency f is slightly below 85 kHz, θ_{in} exhibits a monotonic upward trend and rapidly approaches 90°, thereby leading to an increase in reactive power loss. Conversely, when f is slightly above 85 kHz, θ_{in} displays a monotonic downward trend and rapidly approaches −90°, causing hard-switching operation of the HFI and increasing switching losses.

As shown in Figure 8a,b,e,f, under CC-mode operation, the system characteristics exhibit distinct variations with respect to resonant parameter changes for the two resonant capacitor configurations; however, the parameter sensitivity remains comparable in both cases, rendering it unsuitable for differentiation.

Under CV-mode operation, from Figure 8c,d, it can be observed that, under the first resonant parameter set, C_{r1} and C_{s1} have a certain influence on the input phase angle, whereas the output voltage exhibits relatively high sensitivity only to variations in C_{s1}. As can be seen from Figure 8g,h, under the second resonant parameter set, the input phase angle exhibits high sensitivity to variations in C_{r_2}, C_{2_2}, C_{s_2}, C_{3_2}; in contrast, C_{s_2} and C_{3_2} exert significant influence on the output voltage. As a result, under the CV mode, the system robustness with the first set of resonant parameters is significantly higher than that with the second set of resonant parameters.

From the comparative analysis of the system frequency characteristics and parameter sensitivity under the two sets of resonant parameters described above, it can be concluded that compared with the second set, the system under the first set of resonant parameters provides higher design tolerance and operational stability. Therefore, the first set of resonant parameters is ultimately selected in this paper for constructing the experimental platform and carrying out experimental verification. The specific parameter design process is shown in Figure 9.

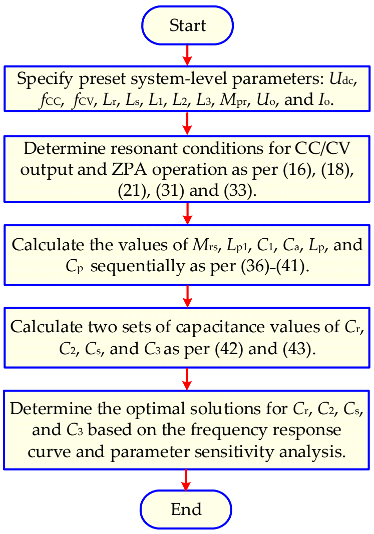

Figure 9. Parameter design flowchart of the proposed compensation topology.

Given that the system objective is to achieve CC/CV hybrid charging, a concise frequency switching control strategy is adopted. Its control logic and specific process are shown in Figures 10 and 11, respectively.

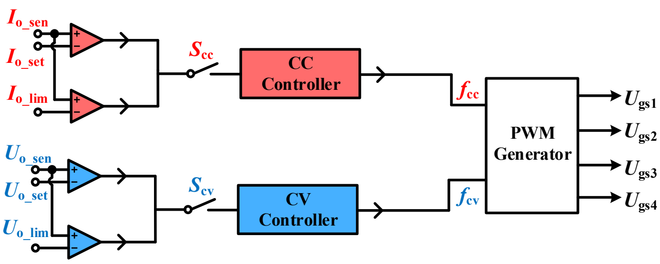

Figure 10. Logic diagram of the dual-frequency WPT system controller.

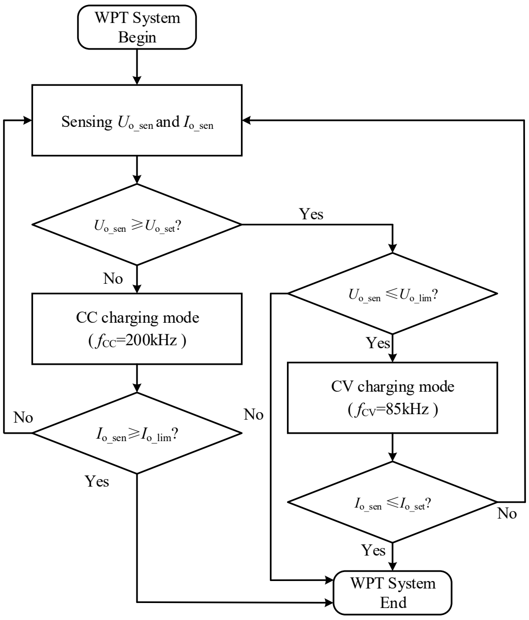

Figure 11. Control flowchart of the dual-frequency WPT system.

As shown in the controller flowchart of the WPT system in Figure 10, when the sampled DC current satisfies $I_{o\_sen} < I_{o\_lim}$ and $I_{o\_sen} > I_{o\_set}$, the CC mode switch is set to $S_{cc} = 1$ and the CV mode switch to $S_{cv} = 0$ to execute the CC controller. The system then outputs four complementary PWM signals at f_{cc} = 200 kHz to enter CC mode. When the sampled DC voltage satisfies $U_{o\_sen} < U_{o\_lim}$ and $U_{o\_sen} > U_{o\_set}$, the CC mode switch is set to $S_{cc} = 0$ and the CV mode switch to $S_{cv} = 1$ to execute the CV controller. The system then outputs four complementary PWM signals at f_{cv} = 85 kHz to enter CV mode.

As shown in the WPT system control flowchart in Figure 11, if the sampled DC voltage satisfies $U_{o\_sen} < U_{o\_set}$, the system operates in CC charging mode; when the sampled DC voltage reaches $U_{o\_sen} \geq U_{o\_set}$, the system operates in CV charging mode. Additionally, if the sampled voltage U_{o_sen} or current I_{o_set} exceeds the preset limit U_{o_lim} or I_{o_lim}, or if I_{o_sen} falls below the preset lower current limit I_{o_set}, the WPT system stops charging.

4. Experimental Verification

Guided by the system configurations listed in Tables 2 and 3, a 400 W experimental setup was implemented to demonstrate the practical viability of the presented scheme. A photograph of this platform is provided in Figure 12.

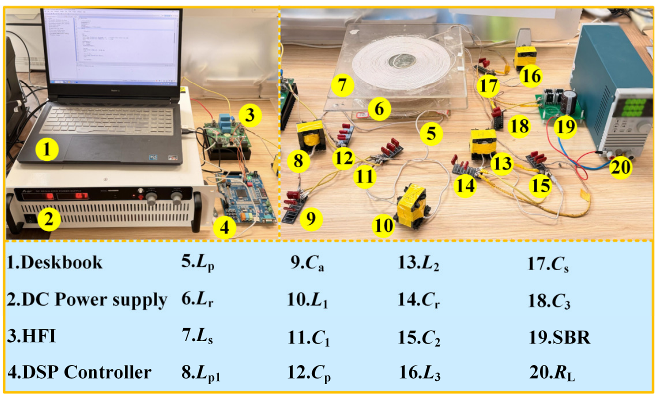

Figure 12. Schematic diagram of the experimental equipment.

In Figure 12, the system employs four C3M0030090K SiC MOSFETs to construct the HFI and four DSA30I100PA Schottky diodes to build the SBR. A TMS320F28335 digital signal processor (DSP) is utilized to implement the overall system control functions. The DC input voltage of the system is set to 200 V, while the DC output current in CC mode and output voltage in CV mode are set to 5 A and 80 V, respectively. Based on the previous analysis, the two resonant frequencies of the system should theoretically be set to f_{cc} = 200 kHz and f_{cv} = 85 kHz, respectively. However, considering that the HFI should operate under ZVS soft-switching conditions during actual system operation to reduce switching losses as shown in Figure 7e, under the first set of resonant parameters, slightly reducing f_c and f_{cv} allows the system input impedance angle to exhibit a slightly inductive characteristic in both CC and CV modes. This guarantees ZVS operation of the HFI across the entire load range. The actual operating frequencies in CC and CV modes are set to 199.3 kHz and 84.7 kHz, respectively. After constructing the experimental prototype, an LCR meter was used to measure the resonant parameters of the coupled coils and the compensation network. The maximum deviation between the measured parameters and the design values was within 3%. The practical system parameters are listed in Table 4.

Table 4. Practical parameters of the WPT system.

Symbols	Parameters	Values
f_{CC}	Resonant frequency1 (for CC mode)	199.3 kHz
f_{CV}	Resonant frequency2 (for CV mode)	84.7 kHz
L_p	Transmitting coil inductance	90.4 µH
L_r	Repeating coil inductance	316.7 µH
L_s	Receiving coil inductance	206.8 µH
M_{pr}	Transmitting and repeating mutual inductance	64.1 µH
M_{rs}	Repeating and receiving mutual inductance	26.3 µH
L_1	Parallel compensation inductance of DFCNa	98.7 µH
L_2	Parallel compensation inductance of DFCNb	101.2 µH
L_3	Parallel compensation inductance of DFCNc	99.1 µH
L_{p1}	Transmitting compensation inductance	64.7 µH
C_1	Transmitting parallel compensation capacitance	35.6 nF
C_a	Transmitting series compensation capacitance	14.7 nF
C_p	Transmitting series compensation capacitance	22.4 nF
C_r	Repeating series compensation capacitance	7.8 nF
C_2	Repeating parallel compensation capacitance	9.1 nF
C_s	Receiving series compensation capacitance	10.2 nF
C_3	Receiving parallel compensation capacitance	10.8 nF

For the purpose of assessing the load-independent CC/CV characteristics alongside the ZPA operation, specific experimental tests incorporating load variations were implemented. A DC electronic load was employed in the experiment to simulate the dynamic resistance variation at the battery terminal during the entire CC/CV charging process, with the load resistance adjustment range specified from 4 Ω to 28 Ω. Figure 13 illustrates the experimental waveforms in CC charging mode. As shown in Figure 13a, as the load resistance increases step by step from 4 Ω to 16 Ω, the output current I_o decreases slightly from

4.98 A to 4.92 A, which agrees well with the theoretical design value of 5 A. Furthermore, the maximum output current ripple ratio in this mode is only 1.2%. Meanwhile, combined with the zoomed-in transient waveforms of the CC mode shown in Figure 13b,c, it can be observed that the system achieves ZPA operation under both light-load and heavy-load conditions. Figure 14 shows the experimental waveforms in CV charging mode.

Figure 13. Experimental waveforms of the system in CC mode (@ alignment condition: ΔX = 0 mm, ΔZ = 0 mm): (**a**) transient waveform when R_L varies from 4 Ω to 16 Ω; (**b**) enlarged waveform when R_L = 4 Ω; (**c**) enlarged waveform when R_L = 16 Ω.

As depicted in Figure 14a, when the load resistance increases step by step from 16 Ω to 28 Ω, the output voltage U_o increases slightly from 79.1 V to 80.3 V, which is consistent with the theoretical design value of 80 V. The maximum output voltage ripple ratio in this mode is 1.5%. Additionally, as can be seen from the zoomed-in CV mode waveforms shown in Figure 14b,c, the system also achieves ZPA operation under both light-load and heavy-load conditions. Comprehensive analysis of the experimental results in Figures 13 and 14 indicates that due to factors such as deviations in actual resonant parameters and equivalent series resistance (ESR) of the circuit, slight deviations exist between the actual DC output current and voltage values and their theoretical design values; however, these deviations remain well within the acceptable error margin. In addition, the charging current I_o in CC mode and the charging voltage U_o in CV mode both remain approximately constant, and stable system operation at the ZPA state is guaranteed in both charging modes. The above experimental results fully verify that the proposed dual-frequency switchable WPT system possesses both load-independent CC/CV output capability and ZPA operating capability.

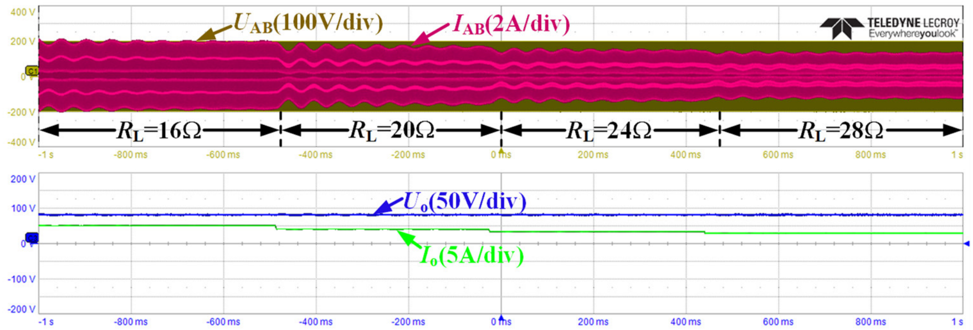

(**a**)

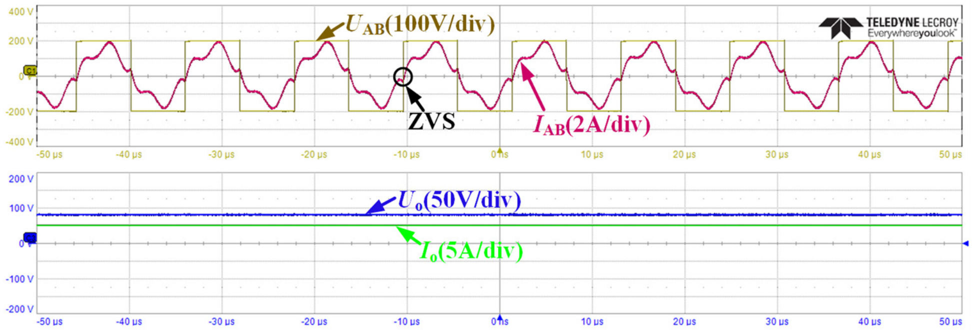

(**b**)

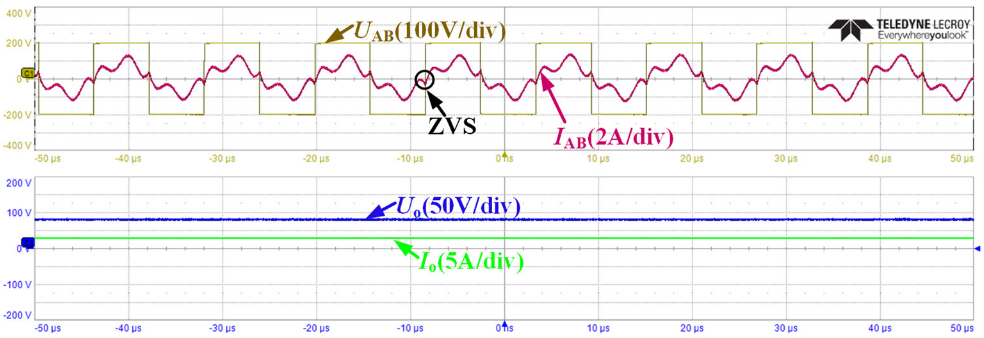

(**c**)

Figure 14. Experimental waveforms of the system in CV mode (@ alignment condition: ΔX = 0 mm, ΔZ = 0 mm): (**a**) transient waveform when R_L varies from 16 Ω to 28 Ω; (**b**) enlarged waveform when R_L = 16 Ω; (**c**) enlarged waveform when R_L = 28 Ω.

To further verify the dynamic switching performance of the designed system from CC mode to CV mode, dynamic CC/CV mode transition experiments were conducted, with the resulting waveform variations shown in Figure 15. During the system load-carrying operation stage, considering that mode transitions are prone to problems such as large current and voltage spikes and system oscillation, a targeted soft-switching charging mode transition method is designed in this paper to solve these issues. The specific operation procedure is as follows: shortly before the mode transition point arrives, the four PWM drive signals of the HFI are first turned off to cut off the power transmission channel. After the controller switches the system operating frequency from the CC mode frequency to the CV mode frequency, the PWM drive signals are re-enabled. Although this operation causes a brief interruption in charging, its impact is negligible compared to the entire charging cycle. As can be seen from the waveform data in Figure 15, throughout the entire mode transition process, the output I_o and U_o remain nearly constant without obvious amplitude jumps. Meanwhile, during the transition, neither power signal spikes nor system oscillations occur, indicating that the designed frequency switching control strategy ensures a smooth transition between the CC and CV charging modes.

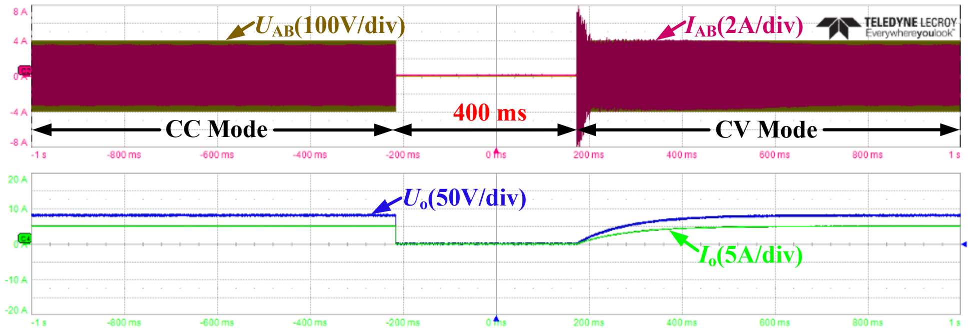

Figure 15. Waveforms of the transition from CC mode to CV mode.

In addition, to validate the operating characteristics of the proposed dual-frequency WPT system under misalignment conditions, the self- and mutual inductances of the coupler are measured and recorded across a range of horizontal and vertical displacements—up to 60 mm horizontally and 15 mm vertically. The results are presented in Figure 16.

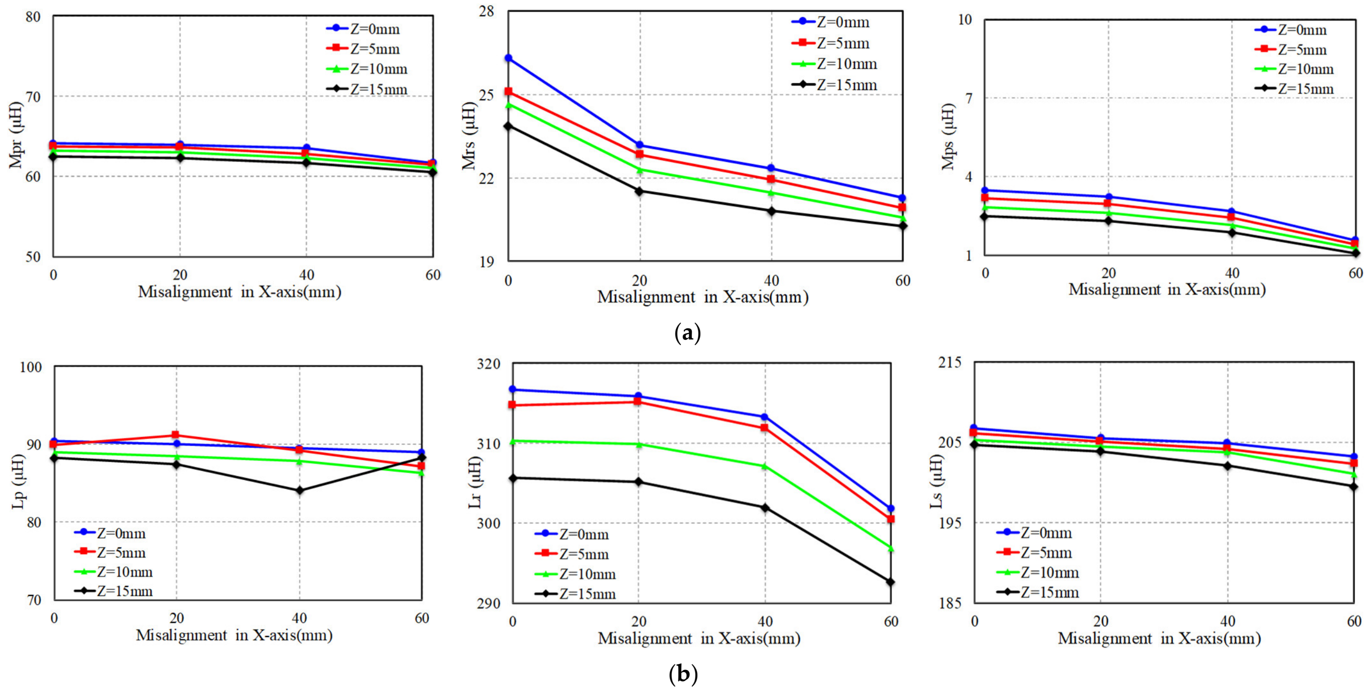

Figure 16. Variation in mutual inductances and self-inductances due to misalignment of receiving coupler. (**a**) Measured mutual inductances (M_{pr}, M_{rs}, M_{ps}). (**b**) Measured self-inductances (L_p, L_r, L_s).

It should be noted that, in practical charging applications—such as mobile desktop charging—the transmitting and repeating coils of a three-coil WPT system are typically integrated into a single power unit, with their relative positions fixed. Therefore, this study focuses exclusively on the misalignment between the receiving and transmitting coils. As shown in Figure 16, all three mutual inductance values of the system decrease monotonically with increasing horizontal and longitudinal offset distances. Among them, M_{pr} exhibits only a marginal reduction, owing to the relatively fixed spatial positions of the transmitting and repeating coils. In contrast, M_{ps}—despite its sensitivity to misalignment—is negligible under detuned conditions, as its initial value under perfect alignment is inherently small. Among them, since the positions of the transmitting and repeating coils are relatively fixed, the reduction in M_{pr} is very slight. For M_{ps}, due to its already small initial value under aligned conditions, its impact on the system under misalignment conditions can be neglected. M_{rs} demonstrates pronounced sensitivity to variations in the coupler's relative position, attaining a minimum value of 292.6 μH at the maximum offset.

Similar to the variation in mutual inductance, the self-inductances L_r and L_s decrease monotonically with increasing X- and Z-axis offsets. In contrast, the self-inductance L_p exhibits a complex, non-monotonic variation with offset; however, at an X-axis offset of 60 mm, the L_p values across all Z-axis offsets converge closely.

The proposed dual-frequency WPT system exhibits relatively significant changes in both the mutual inductance and self-inductance parameters of the coupler under misalignment conditions. These changes may have specific impacts influences on the CC/CV and ZPA characteristics. Given that the parameters of the system coupler change most significantly at the offset point where ΔX = 60 mm and ΔZ = 15 mm, this point is set as the worst-case operating point of the system, and dynamic load-step transient tests are conducted at this point. The test waveforms under CC and CV modes at the worst-case operating point are presented in Figures 17 and 18, respectively.

As shown in Figure 17a, under the operating condition of f_{CC} = 200 kHz, the output current I_o decreases sharply from 9.72 A to 8.28 A as the load resistance increases stepwise from 4 Ω to 16 Ω, indicating that misalignment significantly affects the CC characteristics of the proposed system. Moreover, compared with the standard preset value of I_o, the initial value of I_o under R_L = 4 Ω has increased by 4.72 A. By comparing Figure 17b with Figure 17c, it can be observed that under light-load conditions, the input phase angle is relatively large and decreases as the load resistance increases. This indicates that misalignment also has a certain impact on the ZPA characteristics in CC mode. Nevertheless, as can be seen from Figure 17d, under the worst-case operating point, the proposed WPT system can still achieve ZVS operation at the rated power operating point in CC mode.

As shown in Figure 18a, under the operating condition of f_{CC} =85 kHz, the output voltage U_o increases slightly from 67.11 V to 67.84 V as the load resistance increases stepwise from 4 Ω to 16 Ω, indicating that the CV characteristic of the proposed system is less affected by misalignment. Figure 18b,c show that when the system operates at the worst-case operating point, the variation trend of the input phase angle in CV mode is exactly opposite to that in CC mode. Figure 18d shows the local detail waveform of MOSFET ZVS operation at R_L = 16 Ω in CV mode under misalignment conditions; the proposed WPT system can still achieve ZVS operation at the rated power operating point in CV mode.

Figure 19a illustrates the correlation characteristics between the battery equivalent resistance R_L and the charging current/voltage. The results indicate that as R_L increases, the charging current remains stably maintained at approximately 5 A in CC mode, while the charging voltage stays stably around 80 V in CV mode. Figure 19b illustrates the DC efficiency and charging power curves throughout the entire charging process. The results indicate that the system achieves a peak DC efficiency of 92.75% across the entire operating range, and the maximum output power occurs at the transition critical point between the CC and CV modes.

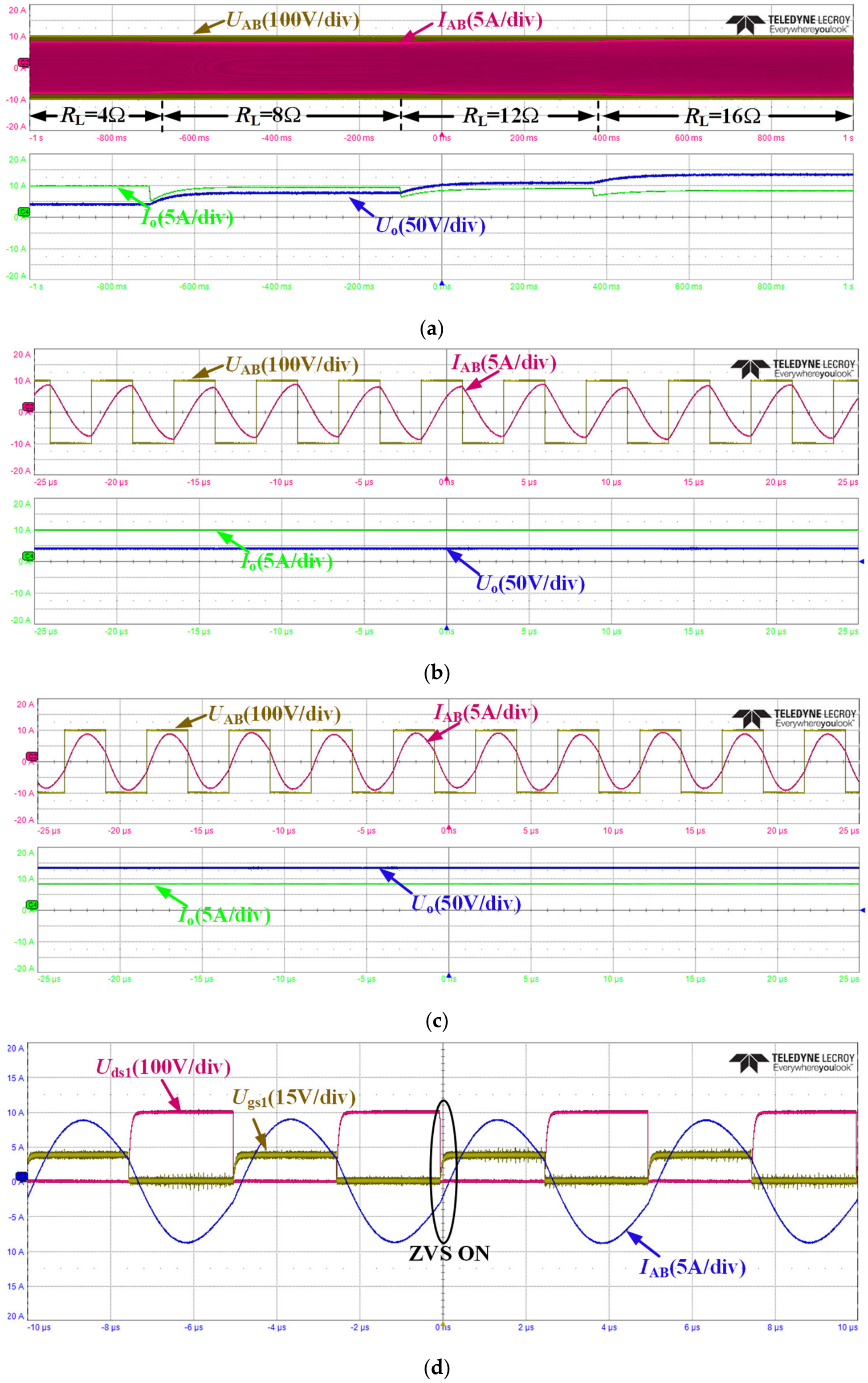

Figure 17. Experimental waveforms of the system in CC mode (@ misalignment condition: ΔX = 60 mm, ΔZ = 15 mm). (**a**) Transient waveform when R_L varies from 4 Ω to 16 Ω; (**b**) enlarged waveform when R_L = 4 Ω; (**c**) enlarged waveform when R_L = 16 Ω; (**d**) local detail waveform of MOSFET ZVS operation at R_L = 16 Ω.

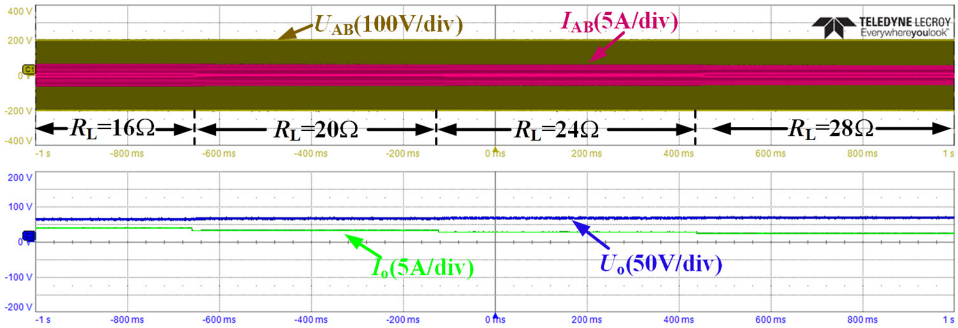

(**a**)

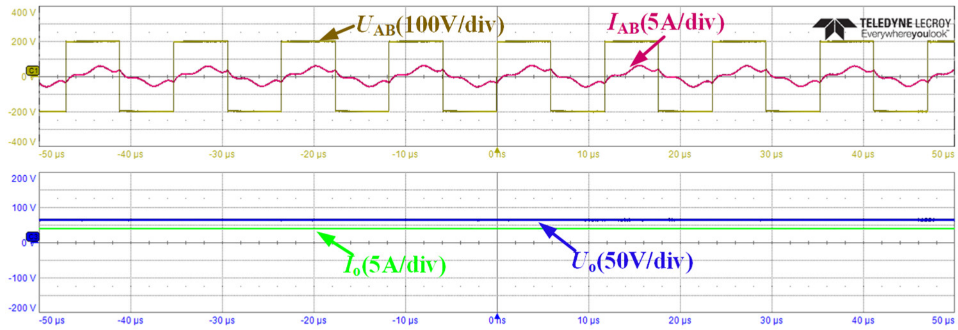

(**b**)

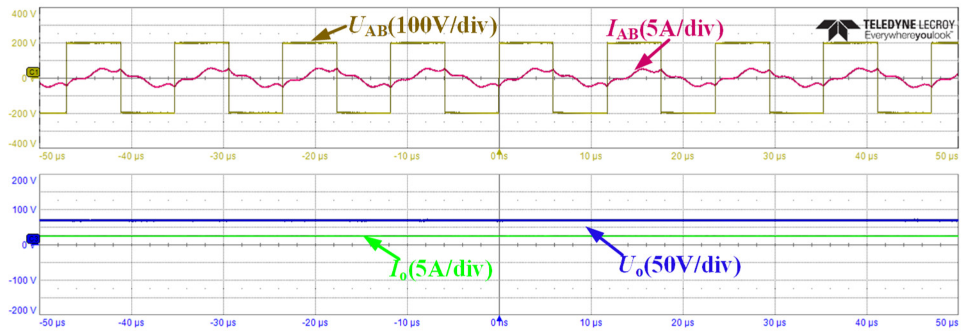

(**c**)

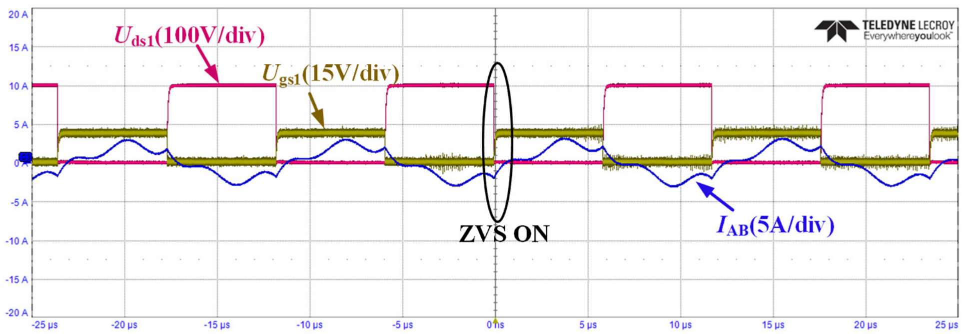

(**d**)

Figure 18. Experimental waveforms of the system in CV mode (@ misalignment condition: ΔX = 60 mm, ΔZ = 15 mm). (**a**) Transient waveform when R_L varies from 16 Ω to 28 Ω; (**b**) enlarged waveform when R_L = 16 Ω; (**c**) enlarged waveform when R_L = 28 Ω; (**d**) local detail waveform of MOSFET ZVS operation at R_L = 16 Ω.

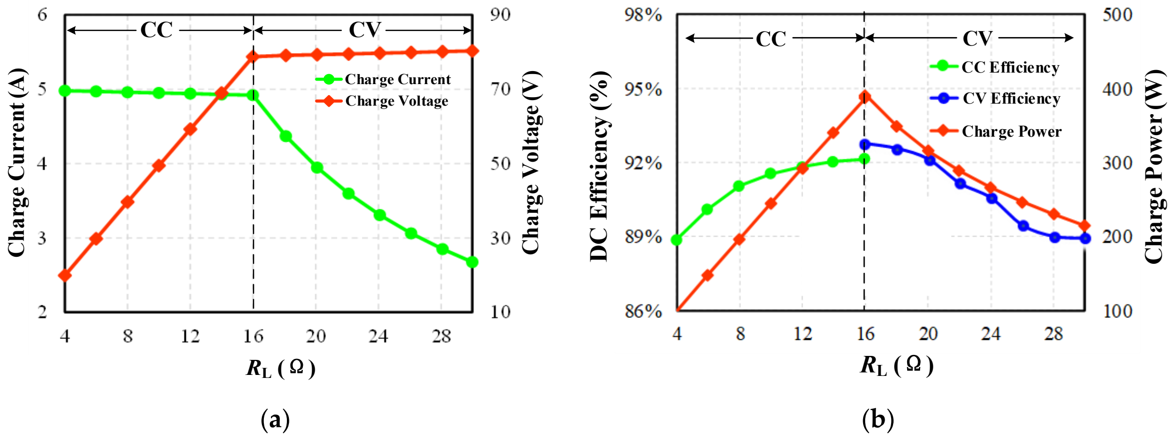

Figure 19. Charging performance of dual-frequency WPT system. (**a**) Measured charge current and voltage; (**b**) measured DC efficiency and charge power.

In addition, to clearly present the practical loss distribution of the dual-frequency WPT system, the system power losses were tested and calculated under light-, medium-, and heavy-load conditions in both CC and CV charging modes. As depicted in Figure 20, at the same output power level, although CC and CV modes exhibit comparable total loss magnitudes, the distinct system parameters and operating characteristics inherent to each charging mode lead to substantial differences in both the distribution profiles and evolution trends of individual loss components across the system.

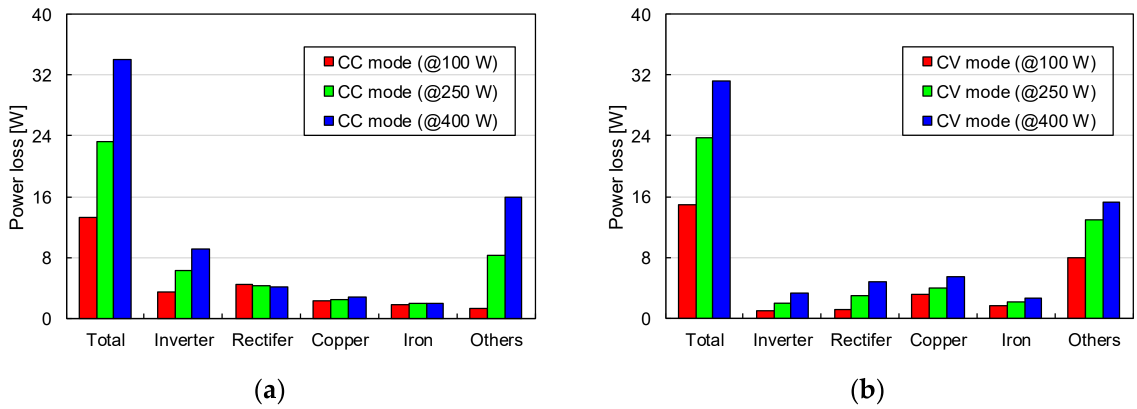

Figure 20. Loss-breakdown diagrams of dual-frequency WC system. (**a**) For CC mode; (**b**) for CV mode.

A comprehensive performance comparison of the proposed topology against the existing three-coil topologies is presented in Table 5. In the three-coil WPT systems reported in [30–34], the conventional compensation topology is reconfigured by incorporating additional AC switches or relays to achieve CC and CV output characteristics, which leads to the increase in system cost, loss and control complexity. Not only that, in [31,32], in order to maintain the ZVS characteristics in CC and CV modes, both the operating frequency and additional switches are controlled synchronously, which leads to a further rise in control complexity. The method proposed in this paper addresses the limitations of the existing approaches listed in Table 5 and achieves certain performance improvements in terms of efficiency, power density, cost, and control complexity.

Table 5. Summary and comparison of the existing three-coil topologies.

Reference	Number of Relays	Peak Efficiency	ZVS Operation	Operating Frequency	Output Property	Topology Structure	Control Complexity	Rating Power
[30]	1	CC: 91.4% CV: 91.9%	Yes	CC: 149.5 kHz CV: 178.7 kHz	CC/CV	LCC-S-S	High	35 W
[31]	2	CC: 87.3% CV: 86.1%	Yes	CC: 85 kHz CV: 175 kHz	CC/CV	S-LCL-S	High	200 W
[32]	2	CC: 90.8% CV: 89.3%	No	CC: 200 kHz CV: 200 kHz	CC/CV	S-S-LCC	Medium	380 W
[33]	1	CC: 91.8% CV: 92.3%	Yes	CC: 85 kHz CV: 85 kHz	CC/CV	S-S-S	Medium	1000 W
[34]	2	CC: 91.2% CV: 89.4%	No	CC: 500 kHz CV: 500 kHz	CC/CV	LC-S-S	Medium	180 W
This article	0	CC: 92.15% CV: 92.75%	Yes	CC: 200 kHz CV: 85 kHz	CC/CV	LCC-S-S	Low	400 W

5. Conclusions

A dual-frequency compatible LCC-S-S and S-S-S compensated three-coil topology is proposed in this paper. Based on the three-coil resonant compensation topology, three DFCNs are employed to replace the compensation capacitors on the transmitter, repeater, and receiver sides, respectively, enabling the topology to be compatible with two distinct resonant frequencies.

Based on the proposed dual-frequency compatible three-coil topology and the characteristic analysis of the DFCN, the resonance conditions for achieving CC/CV output and ZPA operation of the compensation topology are derived, and a general parameter tuning method is proposed. System parameter design is then carried out according to the proposed parameter tuning method.

To address the CC/CV mode switching issue, a soft-switching method for charging mode transition was designed. By switching the operating frequency at the power critical point between the CC and CV charging modes, equivalent switching of the resonant compensation topology between LCC-S-S and S-S-S can be achieved, thereby realizing load-independent CC/CV output and ZPA operation across the full power range. Validation experiments were conducted based on a configured 400 W experimental prototype. The experimental results show that the system can achieve stable CC and CV outputs at the two resonant frequencies, respectively, and the measured values are in high agreement with the theoretical design values. The measured DC efficiencies in CC and CV charging modes reached 92.15% and 92.75%, respectively.

Author Contributions: Conceptualization, Y.C., C.W. and G.L.; methodology, Y.C. and G.L.; validation, C.W. and D.S.; formal analysis, K.W.; investigation, Y.C. and D.-H.K.; writing—original draft preparation, Y.C.; writing—review and editing, C.W. and D.-H.K. All authors have read and agreed to the published version of the manuscript.

Funding: This work was supported by the Science and Technology Key Project in Henan Province under Grant 262102241042 and in part by the National Research Foundation of Korea (NRF) grant funded by the Korean government (MSIT) (RS-2025-00518217).

Data Availability Statement: Data is contained within the article.

Conflicts of Interest: The authors declare no conflicts of interest.

References

1. Ma, T.; Zhu, Z.; Jiang, C.Q.; Ren, S.; Guo, W.; Long, T. GSSA Modeling and Excitation Optimization for Adjacent Coils in Dynamic Wireless Power Transfer Systems. *IEEE Trans. Power Electron.* **2025**, *41*, 8649–8662. [CrossRef]
2. Chen, Y.; Wu, J.; Zhang, H.; Guo, L.; Lu, F.; Jin, N.; Kim, D.H. A parameter tuning method for a double sided LCC compensated IPT system with constant voltage output and efficiency optimization. *IEEE Trans. Power Electron.* **2023**, *38*, 4124–4139. [CrossRef]
3. Dai, J.; Ludois, D.C. A survey of wireless power transfer and a critical comparison of inductive and capacitive coupling for small gap applications. *IEEE Trans. Power Electron.* **2015**, *30*, 6017–6029. [CrossRef]
4. Li, S.; Mi, C.C. Wireless power transfer for electric vehicle applications. *IEEE J. Emerg. Sel. Top. Power Electron.* **2015**, *3*, 4–17. [CrossRef]
5. Sakthi, B.B.; Sundari, P.D. A Wireless Power Transfer (WPT) System for Series-Series Compensation topology in Electric Vehicle Battery Charging Applications. In Proceedings of the 2023 IEEE 8th International Conference for Convergence in Technology (I2CT), Lonavla, India, 7–9 April 2023; pp. 1–4.
6. Lee, H.H.; Kang, S.H.; Jung, C.W. MR-WPT with Reconfigurable Resonator and Ground for Laptop Application. *IEEE Microw. Wirel. Compon. Lett.* **2018**, *28*, 269–271. [CrossRef]
7. Ma, T.; Jiang, C.Q.; Zhou, J.; Chen, C.; Wang, Y.; Zhang, B. Modeling and Analysis of Tetris-Shaped Coils for Dynamic Wireless Power Transfer Systems. *IEEE Trans. Power Electron.* **2026**, *41*, 14290–14304. [CrossRef]
8. Kudaibergenova, Z.; Hashmi, M. Experimental Performance Evaluation of Compact WPT System for Biomedical Applications. In Proceedings of the 2023 Asia-Pacific Microwave Conference (APMC), Taipei, Taiwan, 5–8 December 2023; pp. 447–449.
9. Lv, X.; Dai, X.; Yu, F.; Li, X.; Wang, H.; Sun, Y.; Hu, J. A High Misalignment Tolerance SCC-WPT System with Relay Single Capacitive Coupler for UAV Wireless Charging Applications. *IEEE Trans. Power Electron.* **2025**, *40*, 10372–10377. [CrossRef]
10. Chen, Y.; Zhang, H.; Jin, N.; Guo, L.; Wu, J.; Park, S.-J.; Kim, D.-H. A unipolar-duty-cycle hybrid control strategy of series–series compensated IPT system for constant-current output and efficiency optimization. *IEEE Trans. Power Electron.* **2022**, *37*, 13884–13901. [CrossRef]
11. Li, W.; Zhang, Q.; Cui, C.; Wei, G. A Self-Tuning S/S Compensation WPT System Without Parameter Recognition. *IEEE Trans. Ind. Electron.* **2022**, *69*, 6741–6750. [CrossRef]
12. Chen, Y.; Gao, L.; Liu, K.; Sang, P.; Han, L.; Luan, H.; He, K.; Wu, H. Generic Algorithm Based Parameter Optimization for an S-SP Compensation Topology Based Inductive Power Transfer System. In Proceedings of the 2024 27th International Conference on Electrical Machines and Systems (ICEMS), Fukuoka, Japan, 26–29 November 2024.
13. Xu, F.; Guo, Y.; Zhang, X. An enhanced quasi-CC output model of LCC-P compensated inductive-power-transfer converters. *IEEE Trans. Power Electron.* **2023**, *38*, 15126–15130. [CrossRef]
14. Wang, X.; Leng, M.; He, L.; Lu, S. An Improved LCC-S Compensated Inductive Power Transfer System with Wide Output Voltage Range and Unity Power Factor. *IEEE Trans. Transp. Electrif.* **2024**, *10*, 2342–2354. [CrossRef]
15. Cai, J.; Wu, X.; Sun, P.; Deng, Q.; Sun, J.; Zhou, H. Design of Constant-Voltage and Constant-Current Output Modes of Double-Sided LCC Inductive Power Transfer System for Variable Coupling Conditions. *IEEE Trans. Power Electron.* **2024**, *39*, 1676–1689. [CrossRef]
16. Huang, Z.; Wong, S.-C.; Tse, C.K. Comparison of basic inductive power transfer systems with linear control achieving optimized efficiency. *IEEE Trans. Power Electron.* **2020**, *35*, 3276–3286. [CrossRef]
17. Buja, G.; Bertoluzzo, M.; Mude, K.N. Design and Experimentation of WPT Charger for Electric City Car. *IEEE Trans. Ind. Electron.* **2015**, *62*, 7436–7447. [CrossRef]
18. Berger, A.; Agostinelli, M.; Vesti, S.; Oliver, J.A.; Cobos, J.A.; Huemer, M. A wireless charging system applying phase-shift and amplitude control to maximize efficiency and extractable power. *IEEE Trans. Power Electron.* **2015**, *30*, 6338–6348. [CrossRef]
19. Colak, K.; Asa, E.; Bojarski, M.; Czarkowski, D.; Onar, O.C. A novel phase shift control of semi-bridgeless active rectifier for wireless power transfer. *IEEE Trans. Power Electron.* **2015**, *30*, 6288–6297. [CrossRef]
20. Gati, E.; Kampitsis, G.; Manias, S. Variable frequency controller for inductive power transfer in dynamic conditions. *IEEE Trans. Power Electron.* **2017**, *32*, 1684–1696. [CrossRef]
21. Li, Z.; Xie, B.; Zhu, Y.; Tang, M.; Liu, H.; Guo, X.; Sun, H. Wireless Charging Constant Power Output System Based on LCC/S-S Self-Switching. *IEEE Access* **2022**, *10*, 86435–86444. [CrossRef]
22. Wang, J.; Yu, S.; Huang, Y.; Lin, B.; Liang, G.; Xie, X.; Xie, C. Communication-Free Long-Distance Wireless Charging System for Battery Load with Adaptive Switching of Constant Voltage and Constant Current. *IEEE Trans. Transp. Electrif.* **2024**, *10*, 2653–2662. [CrossRef]
23. Lu, F.; Zhang, H.; Li, W.; Zhou, Z.; Zhu, C.; Cheng, C.; Deng, Z.; Chen, X.; Mi, C.C. A high-efficiency and long-distance power-relay system with equal power distribution. *IEEE J. Emerg. Sel. Top. Power Electron.* **2019**, *8*, 1419–1427. [CrossRef]
24. Cheng, C.; Lu, F.; Zhou, Z.; Li, W.; Deng, Z.; Li, F.; Mi, C.C. A load-independent LCC-compensated wireless power transfer system for multiple loads with a compact coupler design. *IEEE Trans. Ind. Electron.* **2019**, *67*, 4507–4515. [CrossRef]

25. Moon, S.-C.; Moon, G.-W. Wireless power transfer system with an asymmetric four-coil resonator for electric vehicle battery chargers. *IEEE Trans. Power Electron.* **2016**, *31*, 6844–6854. [CrossRef]
26. Darvish, P.; Mekhilef, S.; Illias, H.A.B. A novel S–S–LCLCC compensation for three-coil WPT to improve misalignment and energy efficiency stiffness of wireless charging system. *IEEE Trans. Power Electron.* **2020**, *36*, 1341–1355. [CrossRef]
27. Yao, Z.; Luo, S.; Wei, X.; Zhang, Z.; Li, G.; Shen, X.; Zhang, N.; Krein, P.T.; Ma, H. All-detuned three-coil configuration for advantages in inductive power transfer systems. *IEEE Trans. Power Electron.* **2023**, *38*, 11870–11884. [CrossRef]
28. Liu, X.; Jin, D.; Ji, H.; Liu, L.; Xia, C. Research on mutual inductance identification and efficiency optimization of the three-coil wireless power transfer systems with switchable relay coil. *IEEE Trans. Power Electron.* **2024**, *39*, 6492–6503. [CrossRef]
29. Zhu, J.-Q.; Ban, Y.-L.; Zhang, Y.; Yan, Z.; Xu, R.-M.; Mi, C.C. Three-coil wireless charging system for metal-cover smartphone applications. *IEEE Trans. Power Electron.* **2019**, *35*, 4847–4858. [CrossRef]
30. Wen, H.; Li, J.; Zhang, K.; Wang, P.; Yang, J.; Zhou, X.; Yang, L.; Tong, X.; Song, B. A switchable dual-frequency LCC-S-S compensated three-coil WPT system for mobile desktop charging with constant current and constant voltage outputs. *IEEE Trans. Power Electron.* **2025**, *40*, 7586–7598. [CrossRef]
31. Liu, C.; Zhou, M.; Chen, X.; Zhang, Y. Wireless charging system with dual switchable constant voltage and constant current outputs based on intermediate coils. *IEEE J. Emerg. Sel. Top. Ind. Electron.* **2023**, *5*, 1048–1054. [CrossRef]
32. Li, Y.; Xu, Q.; Lin, T.; Hu, J.; He, Z.; Mai, R. Analysis and design of load-independent output current or output voltage of a three-coil wireless power transfer system. *IEEE Trans. Transp. Electrif.* **2018**, *4*, 364–375. [CrossRef]
33. Zhang, Y.; Shen, Z.; Pan, W.; Wang, H.; Wu, Y.; Mao, X. Constant current and constant voltage charging of wireless power transfer system based on three-coil structure. *IEEE Trans. Ind. Electron.* **2022**, *70*, 1066–1070. [CrossRef]
34. Chen, Y.; Yang, N.; Liu, L.; Dai, R.; He, Z.; Mai, R. Two/Three-coil hybrid topology for WPT systems charging electric bicycles. In Proceedings of the 2019 IEEE Applied Power Electronics Conference and Exposition (APEC), Anaheim, CA, USA, 17–21 March 2019.

https://doi.org/10.3390/electronics15184285